


## RESEARCH ARTICLE

# Momentum-based approximation of incompressible multiphase fluid flows

Loïc Cappanera<sup>1</sup>  | Jean-Luc Guermond<sup>2</sup> | Wietze Herreman<sup>3</sup> | Caroline Nore<sup>3</sup>

<sup>1</sup>Department of Computational and Applied Mathematics, Rice University, 6100 Main MS-134 Houston, TX 77005, USA

<sup>2</sup>Department of Mathematics, Texas A&M University, 3368 TAMU, College Station TX 77843-3368, USA

<sup>3</sup>LIMSI, CNRS, Univ. Paris-Sud, Université Paris-Saclay, Bât 508, rue John von Neumann, Campus Universitaire F-91405 Orsay, France

**Correspondence**

Loïc Cappanera, Department of Computational and Applied Mathematics, Rice University, 6100 Main MS-134, Houston, TX 77005, USA.  
Email: loic.cappanera@gmail.com

**Funding information**

National Science Foundation, Grant/Award Number: DMS-1620058 and DMS-1619892; Air Force Office of Scientific Research, USAF, Grant/Award Number: FA9550-15-1-0257; Army Research Office, Grant/Award Number: W911NF-15-1-0517; GENCI (Grand Equipement National de Calcul Intensif)

**Summary**

We introduce a time stepping technique using the momentum as dependent variable to solve incompressible multiphase problems. The main advantage of this approach is that the mass matrix is time-independent making this technique suitable for spectral methods. A level set method is applied to reconstruct the fluid properties such as density. We also introduce a stabilization method using an entropy-viscosity technique and a compression technique to limit the flattening of the level set function. We extend our algorithm to immiscible conducting fluids by coupling the incompressible Navier-Stokes and the Maxwell equations. We validate the proposed algorithm against analytical and manufactured solutions. Results on test cases such as Newton's bucket problem and a variation thereof are provided. Surface tension effects are tested on benchmark problems involving bubbles. A numerical simulation of a phenomenon related to the industrial production of aluminium is presented at the end of the paper.

**KEYWORDS**

finite elements, incompressible flows, level set method, magnetohydrodynamics, multiphase flows, pseudo-spectral methods

## 1 | INTRODUCTION

Variable density flows and multifluid models are important in many applications ranging from geophysical flows to magnetohydrodynamics (MHD). Almost every solution method for incompressible flows currently available in the literature uses the velocity as dependent variable. This choice has many consequences, and some of them may pose significant difficulties depending on the approximation setting. (1) For instance, denoting the density by  $\rho$  and the velocity by  $\mathbf{u}$ , when using finite elements, the mass matrix associated with the term  $\rho \partial_t \mathbf{u}$  must be assembled at each time step, since the density depends on time and space. The stiffness matrix must also be reassembled if the viscosity depends on  $\rho$ . Changing the mass matrix and the stiffness matrix in turn requires that the linear solver be re-preconditioned regularly as time progresses, which may in some cases be a time-consuming task. (2) Evaluating the product of  $\rho$  by  $\partial_t \mathbf{u}$  can be expensive when using high-order elements. Actually, this product cannot even be made implicit when using spectral methods; that is, it is not possible to use the velocity as dependent variable for spectral methods if  $\rho$  varies in time in large proportions. The objective of this paper is to address the 2 issues above.

In the present paper, we investigate an alternative formulation of the momentum equation, which consists of using the momentum as dependent variable,  $\mathbf{m} := \rho \mathbf{u}$ . Note that this is the approach routinely adopted in compressible fluid mechanics. This change of dependent variable is not simple, since the viscous dissipation depends on the velocity and thereby must be treated implicitly to avoid unreasonable time step restrictions. This obstacle is overcome by rewriting the dissipation appropriately and by accounting for the fact that the range of variation of the kinematic viscosity of many fluids and gases (say  $\nu$ ) is smaller than that of the dynamic viscosity (say  $\eta := \rho \nu$ ). In particular, denoting the symmetric part of the gradient by  $\nabla^s$ , we will rely on the fact that the dominating part of the viscous dissipation operator  $-\nabla \cdot (\eta(\rho) \nabla^s \frac{\mathbf{m}}{\rho})$  can be rewritten as follows:  $-\nabla \cdot (v_{\max} \nabla^s \mathbf{m}) + \nabla \cdot (v_{\max} \nabla^s \mathbf{m} - \eta(\rho) \nabla^s \mathbf{u})$ . Under reasonable simplifying assumptions, it can be shown that provided  $-\nabla \cdot (v_{\max} \nabla^s \mathbf{m})$  is made implicit, the correction  $\nabla \cdot (v_{\max} \nabla^s \mathbf{m} - \eta(\rho) \nabla^s \mathbf{u})$  can be made explicit without compromising unconditional stability too much. This approach has also been used in Dong and Shen.<sup>1</sup> The objectives of the present paper are to develop this idea and to validate the proposed method against referenced cases mainly on hydrodynamical cases. Since the method presented in the paper has been motivated by our current research project in multiphase MHD, we also present at the end of the paper one magnetohydrodynamical application involving conducting liquid metals.

The paper is organized as follows. We formulate the multiphase problem and introduce the level set technique in Section 2. The semi-discretization using the momentum as dependent variable is introduced in Section 3. A stability result in a simplified setting is given. The full discretization is described in Section 4. We show in particular in this section how the level set equation is stabilized by using an entropy-viscosity technique. The proposed technique is validated against analytical and manufactured solutions in Section 5. We solve Newton's bucket problem and a variation thereof in Sections 6 and 7. The modelling of the surface tension effects is validated in Section 8 by solving various classical benchmark problems involving bubbles. Finally, we illustrate the method in the context of MHD with multiphase flows in Section 9 by simulating a metal pad roll (MPR) instability.

## 2 | THE MODEL PROBLEM

We introduce in this section the model problem and describe the level set representation of the 2 phases composing the fluid.

### 2.1 | The Navier-Stokes system

Consider a domain  $D \subset \mathbb{R}^d$ , where  $d = 2$  or  $3$ , occupied by a variable density incompressible fluid. Denoting by  $\rho$ ,  $\mathbf{m}$ , and  $p$  the density, the momentum, and the pressure, the conservation of the mass and the conservation of the momentum are expressed as follows:

$$\partial_t \rho + \nabla \cdot \mathbf{m} = 0, \quad (1a)$$

$$\partial_t \mathbf{m} + \nabla \cdot (\mathbf{m} \otimes \mathbf{u}) - \frac{2}{R_e} \nabla \cdot (\eta(\rho) \varepsilon(\mathbf{u})) + \nabla p = \frac{1}{W_e} \nabla \cdot \mathcal{S} - \frac{1}{F_r} \rho \mathbf{e}_z + \mathbf{f}, \quad (1b)$$

$$\nabla \cdot \mathbf{u} = 0, \quad (1c)$$

where  $\mathbf{u} := \frac{1}{\rho} \mathbf{m}$  is the velocity,  $\varepsilon(\mathbf{u}) := \nabla^s \mathbf{u} = \frac{1}{2}(\nabla \mathbf{u} + (\nabla \mathbf{u})^T)$  is the strain rate tensor, and  $\mathcal{S}$  is the volume distribution of surface tension. The scalar field  $\eta(\rho)$  is the distribution of dynamic viscosity, which we assume to depend on  $\rho$ . The term  $-\frac{1}{F_r} \rho \mathbf{e}_z$  is the buoyancy force; the unit vector  $\mathbf{e}_z$  conventionally gives the upward direction. The quantity  $\mathbf{f}$  is a source term. The above equations are written in nondimensional form. The reference length scale is denoted  $L_{\text{ref}}$ ; the reference velocity is denoted  $U_{\text{ref}}$ ; the reference time scale is then  $L_{\text{ref}}/U_{\text{ref}}$ . The reference density, dynamic viscosity, and surface tension coefficients are denoted  $\rho_{\text{ref}}$ ,  $\eta_{\text{ref}}$ , and  $\kappa_{\text{ref}}$ , respectively. The Reynolds, Froude, and Weber numbers are defined by

$$R_e = \frac{\rho_{\text{ref}} U_{\text{ref}} L_{\text{ref}}}{\eta_{\text{ref}}}, \quad F_r = \frac{U_{\text{ref}}^2}{g L_{\text{ref}}}, \quad W_e = \frac{\rho_{\text{ref}} U_{\text{ref}}^2 L_{\text{ref}}}{\kappa_{\text{ref}}}. \quad (2)$$

The above system is supplemented with initial and boundary conditions

$$\mathbf{u}|_{\partial D} = \mathbf{v}, \quad \mathbf{u}|_{t=0} = \mathbf{u}^0, \quad (3)$$

where  $\partial D$  is the boundary of  $D$ . The initial velocity field  $\mathbf{u}^0$  is assumed to be divergence free.

## 2.2 | Level set representation

We henceforth assume that the fluid is composed of 2 separate phases of (nondimensional) density  $\rho_0, \rho_1$  and dynamic viscosity  $\eta_0, \eta_1$ , and we propose to represent the density distribution by using a level set technique. Compared to front tracking techniques, level set methods have the advantage of handling topology changes of interfaces easily, see eg, literature.<sup>2-5</sup> We then introduce the level set function  $\phi : D \times [0, T] \rightarrow [0, 1]$  satisfying the following transport equation:

$$\partial_t \phi + \mathbf{u} \cdot \nabla \phi = 0, \quad \phi|_{t=0} = \phi^0. \quad (4)$$

The domain is assumed to be closed, and  $\partial D$  is assumed to be a characteristics boundary, ie,  $\mathbf{u} \cdot \mathbf{n}|_{\partial D} = 0$ , which implies that there is no boundary condition on the level set function  $\phi$ . The initial data  $\phi^0$  conventionally takes values in  $[0, 1]$ . The density and the dynamical viscosity are reconstructed by means of the level set function as follows:

$$\rho = \rho_0 + (\rho_1 - \rho_0)F(\phi), \quad \eta = \eta_0 + (\eta_1 - \eta_0)F(\phi). \quad (5)$$

There are many ways available in the literature to define the approximate Heaviside function  $F$ . Two techniques are considered in the present paper: either  $F$  is the identity,  $F(\phi) = \phi$ , and we refer to this method as the linear reconstruction, or  $F$  is the piecewise polynomial function defined by

$$F(\phi) = \begin{cases} 0 & \text{if } \phi - 0.5 \leq -c_{\text{reg}}, \\ \frac{1}{2} \left( 1 + \frac{(\phi - 0.5)((\phi - 0.5)^2 - 3c_{\text{reg}}^2)}{-2c_{\text{reg}}^3} \right) & \text{if } |\phi - 0.5| \leq c_{\text{reg}}, \\ 1 & \text{if } c_{\text{reg}} \leq \phi - 0.5, \end{cases} \quad (6)$$

and we refer to this method as the non-linear reconstruction. The user-defined coefficient  $c_{\text{reg}}$  is selected in the interval  $(0, \frac{1}{2}]$ ;  $c_{\text{reg}} = 0.5$  is a typical value regularly used. Note that the above definitions imply that  $\rho(\mathbf{x}, t) \in [\rho_0, \rho_1]$  and  $\eta(\rho) \in [\eta_0, \eta_1]$  for all  $\mathbf{x} \in D$  and all  $t \in [0, T]$ , since (4) satisfies the maximum principle  $\phi(\mathbf{x}, t) \in [0, 1]$  for all  $\mathbf{x} \in D, t \geq 0$ . We have thoroughly tested the above 2 reconstruction methods but, owing to a compression technique to be explained in Section 4.3, we have observed that the linear and the non-linear reconstructions give similar quantitative results. We mention the non-linear reconstruction (6) only because this method or variations thereof is commonly used in the level set literature, but it is our impression that the nature of the reconstruction is inessential when combined with the compression technique described in Section 4.3. We will clearly state which reconstruction is used in each test case in Sections 5 to 9.

The surface tension tensor  $S$  appearing in the momentum equation (1b) is expressed in terms of the level set function as follows:

$$S = \frac{\nabla \phi \otimes \nabla \phi}{\|\nabla \phi\|_{\ell^2}} - \|\nabla \phi\|_{\ell^2} \mathcal{I}, \quad (7)$$

where  $\mathcal{I}$  is the  $d \times d$  identity matrix and  $\|\cdot\|_{\ell^2}$  is the Euclidean norm.

*Remark 2.1.* The above setting can be generalized for stratification or inclusions of 3 fluids by considering recursive convex combinations as follows:

$$\rho_{01}(\phi_1) := \rho_0(1 - F(\phi_1)) + \rho_1 F(\phi_1), \quad \eta_{01}(\phi_1) := \eta_0(1 - F(\phi_1)) + \eta_1 F(\phi_1), \quad (8)$$

$$\rho = \rho_{01}(\phi_1)(1 - F(\phi_2)) + \rho_2 F(\phi_2), \quad \eta = \eta_{01}(\phi_1)(1 - F(\phi_2)) + \eta_2 F(\phi_2). \quad (9)$$

This extension has been used to study the Tayler instability of liquid metal batteries in Herreman et al.<sup>6</sup> Here, we have assumed that no triple point occurs in the liquid phases to avoid highly nontrivial modelling problems. Moreover, we do not model wetting phenomena.

## 3 | SEMI-DISCRETIZATION IN TIME

We present in this section 2 time stepping algorithms, both inspired from Guermond et al.<sup>7</sup> The first one addresses the question of replacing the velocity by the momentum as dependent variable. The second shows a pressure splitting

technique that requires solving a constant coefficient Poisson equation for the pressure correction instead of solving a variable coefficient Poisson equation as usually done in the literature.

### 3.1 | Constant matrix diffusion on a model problem

We motivate the approach that we are going to adopt later by considering the following model problem where the pressure is absent:

$$\partial_t \mathbf{m} + \frac{1}{2} \mathbf{m} \nabla \cdot \mathbf{u} + \mathbf{u} \cdot \nabla \mathbf{m} - \nabla \cdot (\eta \varepsilon(\mathbf{u})) = \mathbf{g}, \quad \mathbf{m}|_{\partial D} = 0, \quad \mathbf{m}|_{t=0} = \mathbf{m}^0. \quad (10)$$

This equation is the prototype for the momentum equation. Here,  $\rho$  is a given scalar field that may depend on time and space and  $\mathbf{g}$  can be viewed as a source term collecting the pressure gradient and other source terms from (1b). Note that the term  $\frac{1}{2} \mathbf{m} \nabla \cdot \mathbf{u}$  is consistent since  $\nabla \cdot \mathbf{u} = 0$ . The question that we want to address now is that of approximating (10) in time. Let  $\tau > 0$  be a time step, and let us set  $t_n = n\tau$  for  $n \geq 0$ . For any time-dependent function  $\varphi(t)$ , we set  $\varphi^n = \varphi(t_n)$ , and discrete time sequences are denoted by  $\varphi^\tau = \{\varphi^n\}_{n \geq 0}$ . Also to simplify notation, we define the following time-increment operators:

$$\delta^0 \varphi^n := \varphi^n; \quad \delta^1 \varphi^n := \delta \varphi^n := \varphi^n - \varphi^{n-1}; \quad \delta^k \varphi^n := \delta^{k-1} \varphi^n - \delta^{k-1} \varphi^{n-1}, \quad k \geq 1. \quad (11)$$

We then propose the following discretization of (10): for  $n \geq 0$ , set

$$\mathbf{m}^{\#n} := \rho^{n+1} \mathbf{u}^n \quad \text{and} \quad R^{n+1} := \frac{1}{\rho^{n+1}} \left( \frac{\delta \rho^{n+1}}{\tau} + \mathbf{u}^n \cdot \nabla \rho^{n+1} \right), \quad (12)$$

and let  $\mathbf{m}^{n+1}$  be the solution of

$$\frac{\delta \mathbf{m}^{n+1}}{\tau} + \frac{1}{2} \mathbf{m}^{n+1} (\nabla \cdot \mathbf{u}^n - R^{n+1}) + \mathbf{u}^n \cdot \nabla \mathbf{m}^{n+1} - \bar{\nu} \nabla \cdot (\varepsilon(\mathbf{m}^{n+1} - \mathbf{m}^{\#n})) = \nabla \cdot (\eta^{n+1} \varepsilon(\mathbf{u}^n)) + \mathbf{g}^{n+1}, \quad (13)$$

where  $\bar{\nu}$  is a time-independent constant yet to be defined. We assume that the density is computed in such a way that the residual  $R^{n+1}$  is small, ie, the term  $\frac{1}{2} \mathbf{m}^{n+1} (\nabla \cdot \mathbf{u}^n - R^{n+1})$  is consistent. We also assume that the algorithm that produces the approximate density satisfies the maximum principle. More precisely, upon defining  $\rho_{\min} = \text{ess inf}_{\mathbf{x} \in D} \rho^0(\mathbf{x})$  and  $\rho_{\max} = \text{ess sup}_{\mathbf{x} \in D} \rho^0(\mathbf{x})$ , we assume that

$$\rho_{\min} \leq \rho^n \leq \rho_{\max}, \quad \forall n \geq 0. \quad (14)$$

As the dynamical viscosity is seen as a function of the density, we also assume that an analogous inequality can be written for  $\eta^n$ ,  $n \geq 0$ . Many maximum principle preserving finite element methods, second-order accurate and higher, are available in the literature; we refer to Kuzmin et al<sup>8</sup> for a review on some of these methods using the flux transport corrected technology of Boris and Book<sup>9</sup> and Zalesak.<sup>10</sup> Theorem 1 below shows that a good definition for  $\bar{\nu}$  is

$$\bar{\nu} := \|\eta(\rho^0)/\rho^0\|_{L^\infty(D)}, \quad (15)$$

where  $\rho^0$  is the density at the initial time. We adopt this definition in the rest of the paper.

Note that the key advantage of using the momentum as dependent variable is twofold: (1) the mass matrix becomes time-independent and (2) the stiffness matrix associated with the fully discrete version of the algorithm (13) is time-independent.

**Theorem 1.** *Let  $\gamma \in (0, 1)$  be a constant. Assume that the time step is such that  $\tau^{\frac{1}{2}} \bar{\nu} \|\frac{1}{\sqrt{\rho^n \eta^{n+1}}} \nabla \rho^{n+1}\|_{L^\infty(D)} \leq \gamma < 1$  for all  $n \geq 0$  and that the sequence  $\rho^\tau$  is such that  $\bar{\nu} \|\frac{\delta \rho^{n+1}}{\eta^{n+1}}\|_{L^\infty(D)} \leq 1$  for all  $n \geq 0$ . Then the sequence defined by the scheme (13) satisfies the following energy inequality for all  $n \geq 0$ :*

$$\begin{aligned} & \|\sqrt{\rho^{n+1}} \mathbf{u}^{n+1}\|_{L^2(D)}^2 + \tau(1 - \gamma^2) \|\sqrt{\eta^{n+1}} \varepsilon(\mathbf{u}^{n+1})\|_{L^2(D)}^2 + \tau \bar{\nu} \|\sqrt{\rho^{n+1}} \varepsilon(\mathbf{u}^{n+1})\|_{L^2(D)}^2 \\ & \leq \|\sqrt{\rho^n} \mathbf{u}^n\|_{L^2(D)}^2 + \tau \bar{\nu} \|\sqrt{\rho^n} \varepsilon(\mathbf{u}^n)\|_{L^2(D)}^2 + 2\tau \|\mathbf{g}^{n+1}\|_{L^2(D)} \|\mathbf{u}^{n+1}\|_{L^2(D)}, \end{aligned} \quad (16)$$

and there is a constant  $c > 0$ , which only depends on the shape of  $D$ ,  $\eta_{\min}$ , and  $\gamma$ , such that

$$\|\sqrt{\rho^{n+1}}\mathbf{u}^{n+1}\|_{\mathbf{L}^2(D)}^2 \leq \|\sqrt{\rho^0}\mathbf{u}^0\|_{\mathbf{L}^2(D)}^2 + \tau\bar{v}\|\sqrt{\rho^0}\boldsymbol{\varepsilon}(\mathbf{u}^0)\|_{\mathbf{L}^2(D)}^2 + c\tau\sum_{k=0}^n\|\mathbf{g}^{k+1}\|_{\mathbf{L}^2(D)}^2. \quad (17)$$

*Proof.* Let us test the equation with  $2\tau\mathbf{u}^{n+1}$ . Upon noticing that  $\boldsymbol{\varepsilon}(\rho\mathbf{u}) : \boldsymbol{\varepsilon}(\mathbf{v}) \leq \rho\boldsymbol{\varepsilon}(\mathbf{u}) : \boldsymbol{\varepsilon}(\mathbf{v}) + \|\mathbf{u}\|_{\ell^2}\|\nabla\rho\|_{\ell^\infty}\|\boldsymbol{\varepsilon}(\mathbf{v})\|_{\ell^2}$  where  $\|\mathbf{u}\|_{\ell^2}$  is the Euclidean norm of  $\mathbf{u}$ ,  $\|\boldsymbol{\varepsilon}(\mathbf{v})\|_{\ell^2}$  is the induced matrix norm of  $\boldsymbol{\varepsilon}(\mathbf{v})$ , and  $\|\mathbf{w}\|_{\ell^\infty}$  is the max-norm of  $\mathbf{w}$ , we infer that

$$\begin{aligned} 2\int_D\bar{v}\boldsymbol{\varepsilon}(\mathbf{m}^{n+1}-\mathbf{m}^{\#n}) : \boldsymbol{\varepsilon}(\mathbf{u}^{n+1})\,d\mathbf{x} &= 2\int_D\bar{v}\boldsymbol{\varepsilon}(\rho^{n+1}(\mathbf{u}^{n+1}-\mathbf{u}^n)) : \boldsymbol{\varepsilon}(\mathbf{u}^{n+1})\,d\mathbf{x} \\ &\geq 2\int_D\bar{v}\rho^{n+1}\boldsymbol{\varepsilon}(\delta\mathbf{u}^{n+1}) : \boldsymbol{\varepsilon}(\mathbf{u}^{n+1})\,d\mathbf{x} - 2\bar{v}\|\sqrt{\rho^n}\delta\mathbf{u}^{n+1}\|_{\mathbf{L}^2(D)}\|\frac{1}{\sqrt{\rho^n\eta^{n+1}}}\nabla\rho^{n+1}\|_{\mathbf{L}^\infty(D)}\|\sqrt{\eta^{n+1}}\boldsymbol{\varepsilon}(\mathbf{u}^{n+1})\|_{\mathbf{L}^2(D)} \\ &\geq \bar{v}\|\sqrt{\rho^{n+1}}\boldsymbol{\varepsilon}(\mathbf{u}^{n+1})\|_{\mathbf{L}^2(D)}^2 - \bar{v}\|\sqrt{\rho^{n+1}}\boldsymbol{\varepsilon}(\mathbf{u}^n)\|_{\mathbf{L}^2(D)}^2 + \bar{v}\|\sqrt{\rho^{n+1}}\boldsymbol{\varepsilon}(\delta\mathbf{u}^{n+1})\|_{\mathbf{L}^2(D)}^2 \\ &\quad - 2\bar{v}\|\sqrt{\rho^n}\delta\mathbf{u}^{n+1}\|_{\mathbf{L}^2(D)}\|\frac{1}{\sqrt{\rho^n\eta^{n+1}}}\nabla\rho^{n+1}\|_{\mathbf{L}^\infty(D)}\|\sqrt{\eta^{n+1}}\boldsymbol{\varepsilon}(\mathbf{u}^{n+1})\|_{\mathbf{L}^2(D)}. \end{aligned}$$

Moreover, using the following identities

$$\begin{aligned} 2\int_D\delta\mathbf{m}^{n+1}\cdot\mathbf{u}^{n+1}\,d\mathbf{x} &= \|\sqrt{\rho^{n+1}}\mathbf{u}^{n+1}\|_{\mathbf{L}^2(D)}^2 - \|\sqrt{\rho^n}\mathbf{u}^n\|_{\mathbf{L}^2(D)}^2 + \|\sqrt{\rho^n}\delta\mathbf{u}^{n+1}\|_{\mathbf{L}^2(D)}^2 + \int_D\|\mathbf{u}^{n+1}\|_{\ell^2}^2\delta\rho^{n+1}\,d\mathbf{x}, \\ \int_D(\rho^{n+1}\mathbf{u}^{n+1}(\nabla\cdot\mathbf{u}^n - R^{n+1}) + 2\mathbf{u}^n\cdot\nabla\mathbf{m}^{n+1})\cdot\mathbf{u}^{n+1}\,d\mathbf{x} &= \int_D\|\mathbf{u}^{n+1}\|_{\ell^2}^2(\mathbf{u}^n\cdot\nabla\rho^{n+1} - \rho^{n+1}R^{n+1})\,d\mathbf{x}, \\ 2\int_D\eta^{n+1}\boldsymbol{\varepsilon}(\mathbf{u}^n)\boldsymbol{\varepsilon}(\mathbf{u}^{n+1})\,d\mathbf{x} &= -\|\sqrt{\eta^{n+1}}\boldsymbol{\varepsilon}(\delta\mathbf{u}^{n+1})\|_{\mathbf{L}^2(D)}^2 + \|\sqrt{\eta^{n+1}}\boldsymbol{\varepsilon}(\mathbf{u}^{n+1})\|_{\mathbf{L}^2(D)}^2 + \|\sqrt{\eta^{n+1}}\boldsymbol{\varepsilon}(\mathbf{u}^n)\|_{\mathbf{L}^2(D)}^2, \end{aligned}$$

we obtain

$$\begin{aligned} &\|\sqrt{\rho^{n+1}}\mathbf{u}^{n+1}\|_{\mathbf{L}^2(D)}^2 + \|\sqrt{\rho^n}\delta\mathbf{u}^{n+1}\|_{\mathbf{L}^2(D)}^2 + \tau\|\sqrt{\eta^{n+1}}\boldsymbol{\varepsilon}(\mathbf{u}^{n+1})\|_{\mathbf{L}^2(D)}^2 + \tau\|\sqrt{\eta^{n+1}}\boldsymbol{\varepsilon}(\mathbf{u}^n)\|_{\mathbf{L}^2(D)}^2 \\ &\quad + \tau\bar{v}\|\sqrt{\rho^{n+1}}\boldsymbol{\varepsilon}(\mathbf{u}^{n+1})\|_{\mathbf{L}^2(D)}^2 + \tau\bar{v}\|\sqrt{\rho^{n+1}}\boldsymbol{\varepsilon}(\delta\mathbf{u}^{n+1})\|_{\mathbf{L}^2(D)}^2 \leq 2\tau\|\mathbf{g}\|_{\mathbf{L}^2(D)}\|\mathbf{u}^{n+1}\|_{\mathbf{L}^2(D)} \\ &\quad + \|\sqrt{\rho^n}\mathbf{u}^n\|_{\mathbf{L}^2(D)}^2 + \tau\|\sqrt{\eta^{n+1}}\boldsymbol{\varepsilon}(\delta\mathbf{u}^{n+1})\|_{\mathbf{L}^2(D)}^2 + \tau\bar{v}\|\sqrt{\rho^{n+1}}\boldsymbol{\varepsilon}(\mathbf{u}^n)\|_{\mathbf{L}^2(D)}^2 \\ &\quad + 2\tau\bar{v}\|\sqrt{\rho^n}\delta\mathbf{u}^{n+1}\|_{\mathbf{L}^2(D)}\|\frac{1}{\sqrt{\rho^n\eta^{n+1}}}\nabla\rho^{n+1}\|_{\mathbf{L}^\infty(D)}\|\sqrt{\eta^{n+1}}\boldsymbol{\varepsilon}(\mathbf{u}^{n+1})\|_{\mathbf{L}^2(D)}, \end{aligned}$$

where we used that  $\int_D\|\mathbf{u}^{n+1}\|_{\ell^2}^2(\delta\rho^{n+1} + \tau\mathbf{u}^n\cdot\nabla\rho^{n+1} - \tau\rho^{n+1}R^{n+1})\,d\mathbf{x} = 0$ , owing to the definition of  $R^{n+1}$ . The assumed restriction on the time step,  $\tau^{\frac{1}{2}}\bar{v}\|\frac{1}{\sqrt{\rho^n\eta^{n+1}}}\nabla\rho^{n+1}\|_{\mathbf{L}^\infty(D)} \leq \gamma < 1$ , implies that

$$\begin{aligned} &2\tau\bar{v}\|\sqrt{\rho^n}\delta\mathbf{u}^{n+1}\|_{\mathbf{L}^2(D)}\|\frac{1}{\sqrt{\rho^n\eta^{n+1}}}\nabla\rho^{n+1}\|_{\mathbf{L}^\infty(D)}\|\sqrt{\eta^{n+1}}\boldsymbol{\varepsilon}(\mathbf{u}^{n+1})\|_{\mathbf{L}^2(D)}^2 \\ &\leq \|\sqrt{\rho^n}\delta\mathbf{u}^{n+1}\|_{\mathbf{L}^2(D)}^2 + \tau^2\bar{v}^2\|\frac{1}{\sqrt{\rho^n\eta^{n+1}}}\nabla\rho^{n+1}\|_{\mathbf{L}^\infty(D)}^2\|\sqrt{\eta^{n+1}}\boldsymbol{\varepsilon}(\mathbf{u}^{n+1})\|_{\mathbf{L}^2(D)}^2 \\ &\leq \|\sqrt{\rho^n}\delta\mathbf{u}^{n+1}\|_{\mathbf{L}^2(D)}^2 + \gamma^2\tau\|\sqrt{\eta^{n+1}}\boldsymbol{\varepsilon}(\mathbf{u}^{n+1})\|_{\mathbf{L}^2(D)}^2. \end{aligned}$$

Note finally that the definition of  $\bar{v} = \|\eta(\rho^0)/\rho^0\|_{\mathbf{L}^\infty(D)}$  together with the assumption  $\rho_{\min} \leq \rho^{n+1} \leq \rho_{\max}$  implies that

$$\|\sqrt{\eta^{n+1}}\boldsymbol{\varepsilon}(\delta\mathbf{u}^{n+1})\|_{\mathbf{L}^2(D)} \leq \bar{v}\|\sqrt{\rho^{n+1}}\boldsymbol{\varepsilon}(\delta\mathbf{u}^{n+1})\|_{\mathbf{L}^2(D)}.$$

Using the assumption  $\bar{v}\|\frac{\delta\rho^{n+1}}{\eta^{n+1}}\|_{\mathbf{L}^\infty(D)} \leq 1$ , we infer that

$$\begin{aligned} \bar{\nu} \|\sqrt{\rho^{n+1}} \varepsilon(\mathbf{u}^n)\|_{\mathbf{L}^2(D)}^2 &\leq \bar{\nu} \|\sqrt{\rho^n} \varepsilon(\mathbf{u}^n)\|_{\mathbf{L}^2(D)}^2 + \bar{\nu} \left\| \frac{\delta \rho^{n+1}}{\eta^{n+1}} \right\|_{L^\infty(D)} \|\sqrt{\eta^{n+1}} \varepsilon(\mathbf{u}^n)\|_{\mathbf{L}^2(D)}^2 \\ &\leq \bar{\nu} \|\sqrt{\rho^n} \varepsilon(\mathbf{u}^n)\|_{\mathbf{L}^2(D)}^2 + \|\sqrt{\eta^{n+1}} \varepsilon(\mathbf{u}^n)\|_{\mathbf{L}^2(D)}^2. \end{aligned}$$

The inequality (16) follows readily by combining the above estimates. The estimate (17) is a consequence of a standard telescopic argument, the first Korn inequality  $c_1 \|\nabla \mathbf{u}^{n+1}\|_{\mathbf{L}^2(D)} \leq \|\varepsilon(\mathbf{u}^{n+1})\|_{\mathbf{L}^2(D)}$ , the Poincaré inequality  $c_2 \|\mathbf{u}^{n+1}\|_{\mathbf{L}^2(D)} \leq \|\nabla \cdot \mathbf{u}^{n+1}\|_{\mathbf{L}^2(D)}$ , and Young inequality  $2\|\mathbf{g}\|_{\mathbf{L}^2(D)} \|\mathbf{u}^{n+1}\|_{\mathbf{L}^2(D)} \leq \frac{1}{c_3} \|\mathbf{g}\|_{\mathbf{L}^2(D)}^2 + c_3 \|\mathbf{u}^{n+1}\|_{\mathbf{L}^2(D)}^2$ , which holds for all  $c_3 > 0$ . The constant  $c$  in (17) can be chosen to be equal to  $(c_1^2 c_2^2 \eta_{\min} (1 - \gamma^2))^{-1}$ .  $\square$

*Remark 3.1.* While the hypothesis  $\tau^{\frac{1}{2}} \bar{\nu} \left\| \frac{1}{\sqrt{\rho^n \eta^{n+1}}} \nabla \rho^{n+1} \right\|_{L^\infty(D)} \leq \gamma < 1$  may be seen as a CFL-like condition on the time step  $\tau$ , the hypothesis  $\bar{\nu} \left\| \frac{\delta \rho^{n+1}}{\eta^{n+1}} \right\|_{L^\infty(D)} \leq 1$  is far less restrictive. In principle, both conditions can be checked a posteriori and the step  $t_n \rightarrow t_{n+1}$  can be redone with a smaller time step if they are not satisfied.

### 3.2 | Pressure splitting

To avoid the saddle point structure induced by the velocity-pressure coupling, we adopt a splitting technique *à la* Chorin-Temam. However, traditional extension of projection methods, ie, those based on the Helmholtz decomposition  $\mathbf{L}^2(D) = \{\mathbf{v} \in \mathbf{L}^2(D) \mid \nabla \mathbf{v} \in \mathbf{L}^2(D), \mathbf{v} \cdot \mathbf{n}|_{\partial D} = 0\} \oplus \nabla H^1(D)$ , has the disadvantage that the pressure must be computed by solving at each time step an equation of the form

$$-\nabla \cdot \left( \frac{1}{\rho^k} \nabla \Phi \right) = \Psi, \quad (18)$$

which is more time consuming than solving a Poisson problem, see eg, previous studies.<sup>11-14</sup> The algebraic complexity of solving the discrete version of problem (18) is a priori higher than that of a Poisson problem for 2 reasons: (1) the matrix associated with the discrete problem is time-dependent and thus must be reassembled at each time step and (2) the linear system becomes ill-conditioned when the density contrast is high. It is possible to overcome these 2 difficulties without sacrificing stability and accuracy by abandoning the standard projection paradigm as proposed in 2 studies,<sup>15,16</sup> and this is the strategy that we now adopt.

The scheme, inspired from Guermond et al,<sup>7</sup> consists of working with the level set sequence  $\phi^\tau$  plus 4 dependent variables:  $(\rho^\tau, \mathbf{m}^\tau, \psi^\tau, p^\tau)$ , where the sequence  $\rho^\tau$  approximates the density,  $\mathbf{m}^\tau$  the momentum,  $\psi^\tau$  the pressure increment, and  $p^\tau$  the pressure. The density  $\rho^\tau$  and the dynamic viscosity  $\eta^\tau$  are computed from the level set function, and the velocity is defined to be the ratio  $\mathbf{m}^\tau / \rho^\tau$ . The algorithm uses the parameter  $\bar{\nu}$  defined in (15). The proposed algorithm begins with a standard initialization step and proceeds as follows: *Level set*: Set  $\phi^0 = \phi|_{t=0}$ , and for  $n \geq 0$ , compute  $\phi^{n+1}$  by solving

$$\frac{\delta \phi^{n+1}}{\tau} + \mathbf{u}^n \cdot \nabla \phi^n = 0. \quad (19)$$

In all the tests reported below, we do not impose any boundary condition on  $\phi^{n+1}$  when  $\mathbf{u}^n|_{\partial D} \cdot \mathbf{n} = 0$  but we impose a Dirichlet condition on  $\phi^{n+1}$  when  $\mathbf{u}^n|_{\partial D} \cdot \mathbf{n} < 0$ . We reconstruct  $\rho^{n+1}$  and  $\eta^{n+1}$  by setting

$$\rho^{n+1} = \rho_0 + (\rho_1 - \rho_0)F(\phi^{n+1}), \quad \eta^{n+1} = \eta_0 + (\eta_1 - \eta_0)F(\phi^{n+1}). \quad (20)$$

*Momentum*: Set  $\mathbf{m}^0 = \mathbf{m}|_{t=0}$ , and for  $n \geq 0$ , set

$$\mathbf{m}^{\#n} := \rho^{n+1} \mathbf{u}^n, \quad p^{\#,n+1} = p^n + \psi^n \quad \text{and} \quad R^{n+1} := \frac{1}{\rho^{n+1}} \left( \frac{\delta \rho^{n+1}}{\tau} + \mathbf{u}^n \cdot \nabla \rho^{n+1} \right), \quad (21)$$

and let  $\mathbf{m}^{n+1}$  be the solution of

$$\begin{aligned} \frac{\delta \mathbf{m}^{n+1}}{\tau} + \frac{1}{2} \mathbf{m}^{n+1} (\nabla \cdot \mathbf{u}^n - R^{n+1}) + \mathbf{u}^n \cdot \nabla \mathbf{m}^{n+1} - 2 \frac{\bar{\nu}}{Re} \nabla \cdot (\varepsilon(\mathbf{m}^{n+1}) - \mathbf{m}^{\#n}) + \nabla p^{\#,n+1} \\ = \mathbf{f}^{n+1} + \frac{2}{Re} \nabla \cdot (\eta^{n+1} \varepsilon(\mathbf{u}^n)) + \frac{1}{We} \nabla \cdot \left( \frac{\nabla \phi^{n+1} \otimes \nabla \phi^{n+1}}{\|\nabla \phi^{n+1}\|_{\ell^2}} - \|\nabla \phi^{n+1}\|_{\ell^2} \mathbf{I} \right) - \rho^{n+1} \frac{\mathbf{e}_z}{Fr}, \end{aligned} \quad (22)$$

with appropriate boundary conditions on  $\mathbf{u}^{n+1} := \frac{\mathbf{m}^{n+1}}{\rho^{n+1}}$ . In all the tests reported below, we always use Dirichlet boundary conditions on the momentum.

*Penalty:* Compute  $\psi^{n+1}$  by solving

$$\Delta \psi^{n+1} = \frac{\varrho_{\min}}{\tau} \nabla \cdot \mathbf{u}^{n+1}, \quad \partial_n \psi|_{\partial D} = 0. \quad (23)$$

*Pressure update:* Update the pressure

$$p^{n+1} = p^n + \psi^{n+1}. \quad (24)$$

The above algorithm (minus the surface tension and buoyancy terms) has been investigated in Guermond et al<sup>7</sup> and shown therein to be stable under the time step restriction stated in Theorem 1.

## 4 | FULL DISCRETIZATION AND STABILIZATION

We describe the space discretization and the corresponding stabilization techniques in this section.

### 4.1 | Space discretization

Although most of the simulations reported at the end of the paper have been done with a code combining Fourier expansions and finite elements, we describe the fully discrete algorithm using the finite element language to simplify the presentation. Tangential details regarding the handling of the Fourier part of the code are reported in Section 4.5.

Let  $(\mathcal{K}_h)_{h>0}$  be a mesh sequence for the domain  $D \subset \mathbb{R}^d$  that we assume to be matching (no-hanging node) shape regular in the sense of Ciarlet. The reference element is denoted  $\hat{K}$ , and the diffeomorphism mapping  $\hat{K}$  to an arbitrary element  $K \in \mathcal{K}_h$  is denoted  $\Phi_K : \hat{K} \rightarrow K$ . For each mesh cell  $K \in \mathcal{K}_h$ , we define the local mesh size  $h_K$  to be the diameter of the largest ball inscribed in  $K$ . Let  $k, k' \geq 1$  be 2 natural numbers. We define the following spaces:

$$X_h = \{\phi \in C^0(D; \mathbb{R}) \mid \phi|_K \circ \Phi_K \in \mathbb{P}_{k'}, \quad \forall K \in \mathcal{K}_h\}, \quad (25)$$

$$\mathbf{X}_h = \{\mathbf{v} \in C^0(D; \mathbb{R}^d) \mid \mathbf{v}|_K \circ \Phi_K \in \mathbb{P}_k, \quad \forall K \in \mathcal{K}_h\}, \quad (26)$$

$$M_h = \{q \in C^0(D; \mathbb{R}) \mid q|_K \circ \Phi_K \in \mathbb{P}_{k-1}, \quad \forall K \in \mathcal{K}_h\}, \quad (27)$$

where  $\mathbb{P}_k$  is the vector space of polynomials of total degree at most  $k$ . The spaces  $X_h$  and  $M_h$  are composed of scalar-valued functions, whereas  $\mathbf{X}_h$  is composed of vector fields. The pair  $(\mathbf{X}_h, M_h)$  is the so-called Taylor-Hood approximation space, which is known to be stable to approximate the incompressible Navier-Stokes equations. The system of Equations (19) to (24) is discretized by approximating  $\phi^\tau, \rho^\tau, \eta^\tau$  in  $X_h$ ,  $\mathbf{m}^\tau, \mathbf{u}^\tau$  in  $\mathbf{X}_h$ , and  $\psi^\tau, p^\tau, q^\tau$  in  $M_h$ . In the applications reported at the end of the paper, we take  $k = 2$  and either  $k' = 1$  or  $k' = 2$ .

### 4.2 | Stabilization by entropy viscosity

To make time-independent the matrices appearing in the fully discrete version of the discrete level set equation (19) and in the momentum equation (22), the non-linear terms are made explicit and the equations are stabilized by adding some artificial viscosity that we call entropy viscosity.<sup>17</sup> More precisely, we stabilize both equations with an artificial viscosity taken proportional to the default to equilibrium in the mass conservation equation and the kinetic energy equation. First, we compute at each time step and over each mesh cell the residual of the Navier-Stokes equations (22) by setting

$$\mathbf{Res}_{\text{NS}}^n := \frac{\mathbf{m}^n - \mathbf{m}^{n-2}}{2\tau} + \nabla \cdot (\mathbf{m}^{n-1} \otimes \mathbf{u}^{n-1}) - \frac{2}{R_e} \nabla \cdot (\eta^{n-1} \varepsilon(\mathbf{u}^{n-1})) + \nabla p^{n-1} - \mathbf{g}^{n-1}, \quad (28)$$

where  $\mathbf{g}$  takes into account gravity, surface tension, and all other possible source terms. Then we compute the residual of the mass equation (1a) by setting

$$\text{Res}_{\text{mass}}^n := \frac{\rho^n - \rho^{n-2}}{2\tau} + \nabla \cdot (\mathbf{m}^{n-1}). \quad (29)$$



We then define the quantity  $D_{\max}$  by

$$D_{\max|D_K}^n := \max(\|\mathbf{Res}_{\text{NS}}^n \cdot \mathbf{u}^n\|_{\mathbf{L}^\infty(D_K)}, \|\mathbf{Res}_{\text{mass}}^n \mathbf{u}^n \cdot \mathbf{u}^n\|_{\mathbf{L}^\infty(D_K)}), \quad (30)$$

where  $D_K$  is the patch composed of the cells sharing one face with  $K$ . We introduce a local kinematic artificial viscosity defined on each cell  $K$  by setting

$$v_{R|K}^n := \frac{h_K^2 D_{\max|D_K}^n}{\|\mathbf{m}^n \cdot \mathbf{u}^n\|_{\mathbf{L}^\infty(D_K)}}. \quad (31)$$

The quantity  $v_{R|K}^n$  is expected to be as small as the consistency error in regions where the flow and the density distribution are smooth and to be large in the regions where the PDEs are not well resolved. To avoid excessive dissipation and to be able to run with CFL numbers of order  $\mathcal{O}(1)$ , we define the kinematic entropy viscosity  $v_E^n$  as follows:

$$v_{E|K}^n := \min\left(c_{\max} h_K \|\mathbf{u}^n\|_{\mathbf{L}^\infty(D_K)}, c_E v_{R|K}^n\right), \quad (32)$$

with  $c_{\max} = \frac{1}{2}$  for  $\mathbb{P}_1$  finite elements and  $c_{\max} = \frac{1}{8}$  for  $\mathbb{P}_2$  finite elements. The coefficient  $c_E \in (0, 1]$  is tunable, but unless explicitly mentioned, we take  $c_E = 1$  in the simulations reported at the end of the paper. The entropy viscosity  $v_E^n$  is expected to be small in smooth regions and to degenerate to first order in regions with large gradients. Note that  $\frac{1}{2} h_K \|\mathbf{u}^n\|_{\mathbf{L}^\infty(D_K)}$  is the first-order artificial viscosity that corresponds to upwinding in the finite volume and in the finite difference literature.

We explain in the next sections how the viscosity  $v^n$  is used in the mass and momentum conservation equations.

### 4.3 | Compression technique for the level set

Using Euler time stepping to illustrate the method, the mass conservation equation is solved by proceeding as follows: Find  $\phi^{n+1} \in X_h$  such that

$$\int_D \frac{1}{\tau} (\phi^{n+1} - \phi^n) \psi \, dx = - \int_D ((\mathbf{u}^n \cdot \nabla \phi^n) \psi + v_E^n \nabla \phi^n \cdot \nabla \psi) \, dx \quad (33)$$

for all  $\psi \in X_h$ .

To illustrate the efficiency (and some deficiencies) of the entropy viscosity stabilization, we show in Figure 1 solutions of the transport equation  $\partial_t \phi + \partial_x \phi = 0$  over the periodic domain  $(0, 1)$  using continuous piecewise linear finite elements. The entropy viscosity is defined to be  $v_{E|K}^n = \min(\frac{1}{2} h_K, \frac{1}{2} v_{R|K}^n)$  and  $v_{R|K}^n = \|\frac{\delta E(\phi^n)}{\tau} + \partial_x E(\phi^n)\|_{L^\infty(K)}$  with the entropy  $E(\phi) = \log(|\phi(1 - \phi)|)$ . The initial data are  $\phi_0(x) = 1$  if  $0.4 \leq x \leq 0.7$  and  $\phi_0(x) = 0$  otherwise. The mesh is composed of 100 cells, ie, 100 grid points. Three solutions are computed at  $T = 1$ ,  $T = 10$ , and  $T = 100$  in each panel. We show in the left panel the solutions obtained by using the first-order viscosity only, ie,  $v_{E|K} = \frac{1}{2} h_K$ , which can be proved to be equivalent to upwinding in a finite difference context. The method is monotone but very diffusive; actually, it is  $\mathcal{O}(h^{\frac{1}{2}})$  accurate in the  $L^1$ -norm with this particular initial data. The solution computed with the entropy viscosity, ie,  $v_{E|K} = \min(\frac{1}{2} h_K, \frac{1}{2} v_{R|K}^n)$ , is shown in the central panel. The superiority of the entropy viscosity method over the first-order viscosity solution is clear. Note that, although the action of entropy viscosity is mainly localized in the 2 regions where the graph of the solution goes from 0 to 1, the dissipation accumulates in time and the graph of the approximate solution is eventually flattened.

To limit the flattening effect, we introduce a non-linear compression effect in the spirit of the artificial compression methods proposed by Harten.<sup>18</sup> The original idea from Harten was to add an artificial compression step using a false-time iteration after every time step. This antidiffusion step is called reinitialization in the level set literature and is often done by enforcing the level set function to be a signed distance function measuring the distance to the interface of interest. The compression mechanism then consists of making sure that  $\|\nabla \phi\|_{\ell^2} = 1$  after each time step. Solution methods for Hamilton-Jacobi equations are usually used to achieve this goal, see, eg, Sethian.<sup>19</sup> Since it is not really necessary that  $\phi$  be a distance function, we prefer to adopt an approach coming from the shock-capturing literature, such as the artificial compression method of Olsson and Kreiss,<sup>20</sup> and to combine the advection and the so-called reinitialization step into one single time step as done in previous studies.<sup>21,22</sup> Assuming that the level set of interest is  $\{\phi = \frac{1}{2}\}$ , we propose to augment the level set equation with a term proportional to  $\nabla \cdot (\phi(1 - \phi)\mathbf{n})$ , where  $\mathbf{n}$  is a unit vector. The vector  $\mathbf{n}$  is in principle equal



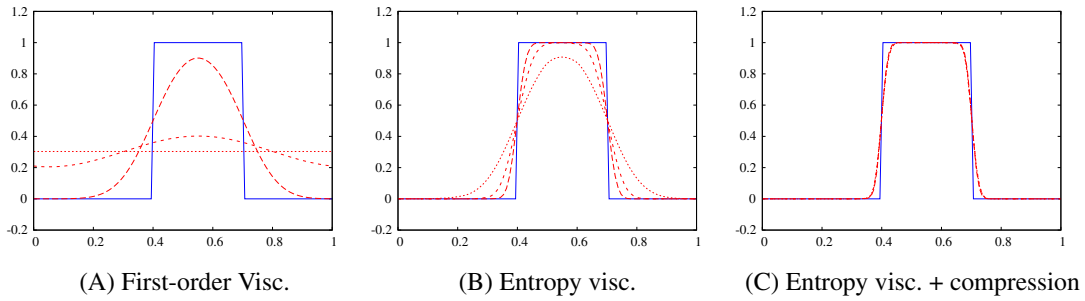


**FIGURE 1** Linear transport: exact and approximate solutions at  $T = 1, 10,$  and  $100$  [Colour figure can be viewed at [wileyonlinelibrary.com](http://wileyonlinelibrary.com)]

to  $\nabla\phi^n/\|\nabla\phi^n\|_{\ell^2}$  on the level set  $\{\phi = \frac{1}{2}\}$ , but since the gradient of  $\phi$  is sensitive to  $\mathcal{O}(h)$  errors, we compute a smooth version thereof by solving  $\phi_{\text{reg}}^n \in X_h$  so that

$$\int_D (w\phi_{\text{reg}}^n + (3h_{\text{reg}})^2 \nabla\phi_{\text{reg}}^n \cdot \nabla w) \, d\mathbf{x} = \int_D w\phi^n \, d\mathbf{x}, \quad \forall w \in X_h, \quad (34)$$

where  $h_{\text{reg}} \in X_h$  is a regularized version of the mesh size. Denoting by  $\{\mathbf{a}_i\}_{1 \leq i \leq I}$ , the collection of the Lagrange nodes associated with the space  $X_h$  and  $\Delta_i = \{K \in \mathcal{K}_h \mid \mathbf{a}_i \in K\}$  the collection of cells containing  $\mathbf{a}_i$ , we define  $h_{\text{reg}} \in X_h$  so that  $h_{\text{reg}}(\mathbf{a}_i) = \frac{1}{\text{card}(\Delta_i)} \sum_K h_K$ . We then approximate the normal  $\mathbf{n}$  by  $\nabla\phi_{\text{reg}}^n/\|\nabla\phi_{\text{reg}}^n\|_{\ell^2}$ . The level set  $\phi^{n+1} \in X_h$  is then computed by enforcing

$$\int_D \frac{\delta\phi^{n+1}}{\tau} w \, d\mathbf{x} = \int_D \left( -w\mathbf{u}^n \cdot \nabla\phi^n - v^n \cdot \left( \nabla\phi^n - \frac{c_{\text{comp}}}{h_{\text{reg}}} \phi^n (1 - \phi^n) \frac{\nabla\phi_{\text{reg}}^n}{\|\nabla\phi_{\text{reg}}^n\|} \right) \cdot \nabla w \right) \, d\mathbf{x}, \quad (35)$$

for all  $w \in X_h$ , where  $c_{\text{comp}}$  is a tunable constant that we choose in the interval  $[0, 1]$ . Unless explicitly mentioned otherwise, we take  $c_{\text{comp}} = 1$  in the simulations reported at the end of the paper. Note in passing that, taking  $w = 1$  in (35) and using the slip boundary condition  $\mathbf{u}_{\partial D}^n \cdot \mathbf{n} = 0$ , we obtain that  $\int_D \phi^{n+1} \, d\mathbf{x} = \int_D \phi^n \, d\mathbf{x}$ ; that is, the total mass of the level set is conserved irrespective of the tuning parameters  $h_{\text{reg}}$  and  $c_{\text{comp}}$ . Other details regarding this technique can be found in Guermond et al.<sup>23</sup>

Let us interpret the effect of the compression on the PDE corresponding to (35). Let  $\mathbf{x}_0(t)$  be a point on the moving interface and assume that  $\phi = \phi_{\text{reg}}$ , the velocity is locally constant in a neighbourhood of  $\mathbf{x}_0$ , and  $\phi(\mathbf{x} - \mathbf{u}t)$  is time-independent. Then denoting  $\varphi(\mathbf{x}) := \phi(\mathbf{x} - \mathbf{u}t)$  and letting  $s$  be the signed distance along the normal direction,  $\varphi$  solves the following ODE,  $\partial_s \varphi + \alpha\varphi(1 - \varphi) = 0$ ,  $\varphi(0) = \frac{1}{2}$ , where  $\alpha = c_{\text{comp}} h_{\text{reg}}^{-1}$ . The solution is  $\varphi(s) = \frac{1}{2} \left( 1 + \tanh \left( c_{\text{comp}} \frac{s}{h_{\text{reg}}} \right) \right)$ . Hence, at equilibrium, the compression balances exactly the artificial viscosity, and the level set adopts the classical hyperbolic tangent profile of width  $h_{\text{reg}}/c_{\text{comp}}$ . This phenomenon is well illustrated in Figure 1C.

Once  $\phi^{n+1}$  is computed, the fluid's physical properties are updated by setting

$$\rho^{n+1} = \rho_0 + (\rho_1 - \rho_0)F(\phi^{n+1}), \quad \eta^{n+1} = \eta_0 + (\eta_1 - \eta_0)F(\phi^{n+1}), \quad (36)$$

where  $F$  is either the linear reconstruction or the non-linear reconstruction defined in Section 2.2. In applications, we have observed that the compression method is very efficient and thus makes the choice of the reconstruction method inessential. We are going to use indifferently one or the other reconstruction method in the tests reported below.

#### 4.4 | Momentum equation and pressure correction

Once the density and the viscosity are estimated, we compute the momentum by solving the following problem: Find  $\mathbf{m}^{n+1} \in \mathbf{X}_h$  such that:

$$\begin{aligned}
& \int_D \left( \frac{1}{\tau} (\mathbf{m}^{n+1} - \mathbf{m}^n) \cdot \mathbf{v} + 2 \frac{\bar{v}}{R_e} \varepsilon(\mathbf{m}^{n+1} - \mathbf{m}^n) : \varepsilon(\mathbf{v}) \right) \mathrm{d}\mathbf{x} \\
& = \int_D \left( -\mathbf{v} \cdot \nabla(p^n + \psi^n) - \nabla \cdot (\mathbf{m}^n \otimes \mathbf{u}^n) \cdot \mathbf{v} - 2 \frac{\eta^n}{R_e} \varepsilon(\mathbf{u}^n) : \varepsilon(\mathbf{v}) - v_E^n \nabla \mathbf{m}^n : \nabla \mathbf{v} \right) \mathrm{d}\mathbf{x} \\
& + \int_D \left( \left( \mathbf{f}^{n+1} - \frac{1}{F_r} \rho^{n+1} \mathbf{e}_z \right) \cdot \mathbf{v} - \frac{1}{W_e} \left( \frac{\nabla \phi^{n+1} \otimes \nabla \phi^{n+1}}{\|\nabla \phi^{n+1}\|_{\ell^2}} - \|\nabla \phi^{n+1}\|_{\ell^2} \mathbf{I} \right) : \varepsilon(\mathbf{v}) \right) \mathrm{d}\mathbf{x},
\end{aligned} \tag{37}$$

for all  $\mathbf{v} \in \mathbf{X}_h$ . The fields  $\psi^{n+1}, p^{n+1}$  are computed by solving the discrete weak form (23) as follows. Find  $\psi^{n+1} \in M_h$  such that

$$\int_D \nabla \psi^{n+1} \cdot \nabla w \mathrm{d}\mathbf{x} = \frac{\rho_{\min}}{\tau} \int_D w \nabla \cdot \mathbf{u}^{n+1} \mathrm{d}\mathbf{x}, \quad \forall w \in M_h, \tag{38}$$

and find  $p^{n+1} \in M_h$  such that

$$\int_D p^{n+1} w \mathrm{d}\mathbf{x} = \int_D (p^n + \psi^{n+1}) w \mathrm{d}\mathbf{x}, \quad \forall w \in M_h. \tag{39}$$

#### 4.5 | Finite elements/Fourier expansion

The algorithms described above are implemented in a code called SFEMaNS, which the authors have been developing since 2003 in the context of a collaborative research programme in MHD. The space discretization is hybrid and specialized to axisymmetric domains. It uses a Fourier decomposition in the azimuthal direction and the standard Taylor-Hood Lagrange elements  $\mathbb{P}_2\text{-}\mathbb{P}_1$  in the meridian section (with  $\mathbb{P}_1$  approximation for the pressure,  $\mathbb{P}_2$  approximation for the velocity field, and either  $\mathbb{P}_1$  or  $\mathbb{P}_2$  approximation for the magnetic field and the level set). The meridian mesh is composed of quadratic triangles.

The level set is approximated by using (35). The physical properties are reconstructed by using (36). The momentum and the pressure are computed by solving (37) to (39). The non-linear terms are made explicit and approximated using second-order extrapolation in time. The non-linear products are computed using a pseudo-spectral method, and the fast Fourier transform subroutines from the FFTW3 package from Frigo and Johnson.<sup>24</sup> The zero-padding technique (2/3-rule) is applied to prevent aliasing. The code is parallelized in the Fourier space by using Message Passing Interface (MPI), and it is parallelized in the meridian section by using the code METIS from Karypis and Kumar<sup>25</sup> for the domain decomposition, and PETSC (Portable, Extensible Toolkit for Scientific Computation)<sup>26</sup> for the parallel linear algebra. We refer to 3 studies<sup>27-29</sup> for more details on SFEMaNS.

#### 4.6 | Extension of the algorithm to the MHD setting

At the end of the paper, we are going to illustrate the method on the resistive MHD equations. The MHD system is written as follows:

$$\partial_t \rho + \nabla \cdot \mathbf{m} = 0, \tag{40}$$

$$\nabla \cdot \mathbf{u} = 0, \tag{41}$$

$$\partial_t \mathbf{m} + \nabla \cdot (\mathbf{m} \otimes \mathbf{u}) - \frac{2}{R_e} \nabla \cdot (\eta \varepsilon(\mathbf{u})) + \nabla p = \frac{1}{W_e} \nabla \cdot \mathbf{S} - \frac{1}{F_r} \rho \mathbf{e}_z + A (\nabla \times \mathbf{b}) \times \mathbf{b}, \tag{42}$$

$$\nabla \cdot \mathbf{b} = 0, \tag{43}$$

$$\partial_t \mathbf{b} + \frac{1}{R_e^m} \nabla \times \left( \frac{1}{\sigma} \nabla \times \mathbf{b} \right) = \nabla \times (\mathbf{u} \times \mathbf{b}), \tag{44}$$

where  $\mathbf{b}$  is the magnetic induction and  $A(\nabla \times \mathbf{b}) \times \mathbf{b}$  the Lorentz force. Two new nondimensional parameters appear: the magnetic Reynolds number  $R_e^m = \mu_0 \sigma_{\text{ref}} L_{\text{ref}} U_{\text{ref}}$ , which characterizes the ratio of the magnetic advection to the magnetic

diffusion, and the coupling parameter  $A = \frac{B_{\text{ref}}^2}{\mu_0 \rho_{\text{ref}} U_{\text{ref}}^2}$ , which measures the ratio of the magnetic energy to the kinetic energy. Note that we only consider problems with constant magnetic permeability  $\mu = \mu_0$  in the present paper. The key point here is that the electrical conductivity  $\sigma$  in the fluids is allowed to vary. The resistivity,  $\frac{1}{\sigma}$ , is reconstructed with the level set and the function  $F$  defined in (6). As in the fully discrete form of the momentum equation (37), the diffusive term in the induction equation is rewritten:  $\nabla \times (\frac{1}{\bar{\sigma}} \nabla \times \mathbf{b}) - \nabla \times ((\frac{1}{\bar{\sigma}} - \frac{1}{\sigma}) \nabla \times \mathbf{b})$  with  $\bar{\sigma} \leq \sigma_{\text{min}}$ . The term  $\nabla \times (\frac{1}{\bar{\sigma}} \nabla \times \mathbf{b})$  is made implicit, whereas the term with variable conductivity  $-\nabla \times ((\frac{1}{\bar{\sigma}} - \frac{1}{\sigma}) \nabla \times \mathbf{b})$  is made explicit to make the stiffness matrix of the problem time-independent and avoid the dependence of  $\sigma$  with respect to the azimuth.

## 5 | ANALYTICAL TESTS

We test the accuracy of the above algorithm (35)-(39), using either manufactured solutions or problems with analytical solutions.

### 5.1 | Smooth manufactured solution

In the first test, we use a manufactured solution to evaluate the convergence properties of the above algorithm with respect to the time step and the mesh size. Using the cylindrical coordinates,  $(r, \theta, z)$ , the computational domain is the cylinder  $D = \{(r, \theta, z) \in [0, 1] \times [0, 2\pi) \times [-1, 1]\}$  and the analytical solution is defined by

$$\phi(r, \theta, z, t) = \frac{1}{2}(r^2 + z^2), \quad \eta(\rho) = \rho, \quad \mathbf{u}(r, \theta, z, t) = (0, r^2 \sin(t - z), 0)^T, \quad p = 0.$$

The reconstruction is linear, ie,  $F(\phi) = \phi$ , so the density is equals to  $\rho = \rho_0 + \Delta\rho \frac{1}{2}(r^2 + z^2)$ , where  $\Delta\rho := \rho_1 - \rho_0$ . The source term  $\mathbf{f}$  is computed accordingly:

$$\mathbf{f} = (-\rho r^3 \sin^2(t - z), \rho r^2 \cos(t - z) + R_e^{-1}(\rho(r^2 - 3)) \sin(t - z) - \Delta\rho r^2(\sin(t - z) - z \cos(t - z)), 0)^T.$$

The surface tension and the buoyancy effects are not accounted for, ie,  $W_e = F_r = \infty$ . We use  $R_e = 250$ ,  $\rho_0 = 1$ , and we run 2 series of simulations: one series is done with  $\rho_1 = 2$ , and the other one is done with  $\rho_1 = 500$ .

The tests are performed on 5 different grids composed of triangular meshes of typical mesh size  $h \in \{0.1, 0.05, 0.025, 0.0125, 0.00625\}$ . We use only the Fourier mode  $m = 0$  since the solution is axisymmetric. The time step is chosen by using the rule  $\tau = 0.1/h$ . The computations are done with  $c_{\text{comp}} = 0$  since there is no interface to preserve here. We take  $c_E = 1$ . The errors on the velocity, the level set, and the pressure in the  $L^2$ -norm at time  $t = 1$  are reported in Tables 1 and 2. All the errors are relative to the corresponding norm of the exact solution. The  $L^2$ -norm of the error on the pressure is normalized by the square root of the volume of  $D$  to avoid division by zero since the exact pressure is zero. We use the Taylor-Hood  $\mathbb{P}_2/\mathbb{P}_1$  element for the velocity and the pressure.

The results shown in Table 1 have been obtained with  $\mathbb{P}_1$  approximation for the level set and BDF1 time stepping both in the level set equation and in the momentum equation. These results are compatible with the theoretical rate  $\mathcal{O}(h^2 + \tau)$

**TABLE 1** Convergence tests using BDF1 and level set  $\mathbb{P}_1$  with  $\tau = h/10$  and  $n_{\text{df}}$  degrees of freedom for the level set

	$L^2$ -Norm of error		Velocity		Pressure		Level set	
	$h$	$n_{\text{df}}$	Error	Rate	Error	Rate	Error	Rate
$\rho_1 = 2$	0.1	270	2.22E-3	-	5.03E-4	-	1.98E-2	-
	0.05	986	7.90E-4	1.60	2.14E-4	1.32	2.19E-3	3.40
	0.025	3810	3.66E-4	1.14	1.04E-4	1.07	4.17E-4	2.46
	0.0125	14993	1.82E-4	1.02	5.16E-5	1.02	1.13E-4	1.90
	0.00625	59628	5.80E-5	1.65	1.65E-5	1.65	3.06E-5	1.89
$\rho_1 = 500$	0.1	270	1.20E-2	-	9.12E-2	-	5.69E-2	-
	0.05	986	1.48E-3	2.99	3.88E-2	1.32	9.75E-3	2.72
	0.025	3810	3.96E-4	1.96	1.43E-3	1.48	1.43E-3	2.84
	0.0125	14993	1.77E-4	1.18	6.72E-3	1.10	1.20E-4	3.61
	0.00625	59628	5.63E-5	1.66	2.14E-3	1.66	3.09E-5	1.96

**TABLE 2** Convergence tests using BDF2 and level set  $\mathbb{P}_2$  with  $\tau = h/10$  and  $n_{df}$  degrees of freedom for the level set

	<b>L<sup>2</sup>-Norm of error</b>		<b>Velocity</b>		<b>Pressure</b>		<b>Level set</b>	
	$h$	$n_{df}$	Error	Rate	Error	Rate	Error	Rate
$\rho_1 = 2$	0.1	1017	1.14E-5	–	3.79E-6	–	2.31E-4	–
	0.05	3821	2.43E-6	1.17	9/30E-7	1.06	8.21E-5	0.78
	0.025	14997	5.59E-7	2.15	2.31E-7	2.04	2.82E-5	1.55
	0.0125	59489	1.35E-7	2.06	5.77E-8	2.01	9.16E-6	1.64
	0.00625	237549	1.39E-9	3.28	5.90E-9	3.29	2.80E-6	1.71
$\rho_1 = 500$	0.1	1017	1.29E-5	–	6.88E-4	–	2.40E-4	–
	0.05	3821	2.69E-6	2.37	1.70E-4	2.11	8.42E-5	1.58
	0.025	14997	6.48E-7	2.08	4.28E-5	2.01	2.88E-5	1.57
	0.0125	59489	1.60E-7	2.03	1.07E-5	2.01	9.28E-6	1.64
	0.00625	237549	1.64E-8	3.29	1.10E-6	3.30	2.84E-6	1.72

corresponding to  $\mathbb{P}_1$  approximation in space and BDF1 time stepping. The error is mainly dominated by the time error. We have verified (tests not reported here) that using  $\tau \sim h^2$  gives second-order accuracy on all the quantities.

The results shown in Table 2 have been obtained with  $\mathbb{P}_2$  approximation for the level set and BDF2 time stepping both in the level set equation and in the momentum equation. These results are compatible with the theoretical rate  $\mathcal{O}(h^3 + \tau^2)$  for the velocity and the level set and  $\mathcal{O}(h^2 + \tau^2)$  for the pressure. We have verified (tests not reported here) that the method is  $\mathcal{O}(h^3)$  on the velocity and the level set by using the scaling  $\tau \sim h^{3/2}$ . This series of tests shows that the proposed algorithm behaves exactly as expected with smooth solutions. All the computations reported in the rest of the paper are done with the  $\mathbb{P}_2$  approximation for the level set.

## 5.2 | Nonsmooth manufactured solution

We now test a nonsmooth manufactured solution defined as follows in the computational domain  $D = \{(r, \theta, z) \in [0, 1] \times [0, 2\pi] \times [-1, 1]\}$ :

$$\phi(r, \theta, z, t) = \begin{cases} 0 & z > t - \frac{1}{2} \\ 1 & z < t - \frac{1}{2} \end{cases}, \quad \mathbf{u}(r, \theta, z, t) = (0, r^2 \sin(t - z), 1)^T, \quad p = 0.$$

The density is obtained by the expression  $\rho = 1 + \phi$ . The surface tension and the buoyancy effects are not accounted for, ie,  $W_e = F_r = \infty$ , but the following source term  $\mathbf{f}$  is added on the right-hand side of the momentum equation:

$$\mathbf{f} = (-\rho r^3 \sin^2(t - z), \frac{r^2 - 3}{R_e} \sin(t - z), 0)^T.$$

We take  $R_e = 250$  and  $\eta := 1$ . Note that the level set and the momentum are discontinuous; hence, the best convergence rate one should expect in the  $L^1$ -norm for these quantities is first-order in space.

We use the same meshes as those used in Section 5.1. The approximation of the level set is done with  $\mathbb{P}_2$  elements. The time step is set by the expression  $\tau = 0.1 \times h/2$ ; the factor 2 accounts for the fact that the maximum speed in the flow is 2. We take  $c_{\text{comp}} = 1$  and  $c_E = 1$ . We report in Table 3 the error in the  $L^2$ -norm on the velocity, the error in the  $L^2$ -norm on the pressure, and the error in the  $L^1$ -norm on the density. All the errors are computed at  $t = 1$  and are relative to the corresponding norm of the exact solution.

**TABLE 3** Convergence tests for nonsmooth solution, using BDF2 and  $\mathbb{P}_2$  level set with  $\tau = 0.1 \times h/2$ 

$h$	$n_{df}$	<b>Velocity, L<sup>2</sup>-Norm</b>		<b>Pressure, L<sup>2</sup>-Norm</b>		<b>density, L<sup>1</sup>-Norm</b>	
		Error	Rate	Error	Rate	Error	Rate
0.1	1017	6.11E-2	–	5.97E-2	–	1.38E-1	–
0.05	3821	4.25E-3	4.03	9.71E-4	6.22	7.43E-2	0.94
0.025	14997	1.23E-3	1.82	5.45E-4	0.84	4.15E-2	0.85
0.0125	59489	4.14E-4	1.58	3.50E-4	0.64	2.48E-2	0.75
0.00625	237549	1.39E-4	1.57	1.67E-4	1.07	1.24E-2	1.00

We observe that the convergence rate for the velocity is 1.5 in the  $\mathbf{L}^2$ -norm; it is 1 for the pressure in the  $L^2$ -norm; it is 1 for the density in the  $L^1$ -norm. These rates are compatible with what one should expect. Note in passing that the method is stable under the usual CFL restriction; that is, the theoretical time step restriction stated in Theorem 1 is probably not optimal (ie, it is too restrictive).

### 5.3 | Gravity waves

We consider a cylinder filled with 2 immiscible fluids of density  $\rho_0 > \rho_1$ . The light fluid of density  $\rho_1$  is on top of the heavier fluid of density  $\rho_0$ . The 2 fluids are initially at rest with interface  $\{z = 0\}$ . The height of the top and the bottom layers of fluid are  $H_1$  and  $H_0$ , respectively; the radius of the vessel is 1. In the regime of infinitesimal displacements and zero viscosity ( $Re \rightarrow +\infty$ ), the motion of the fluid is described by the system

$$\rho_i \partial_t \mathbf{u}_i + \nabla p_i = -\rho_i g \nabla z, \quad \nabla \cdot \mathbf{u}_i = 0, \quad \mathbf{u}_i \cdot \mathbf{n}|_{\partial D} = 0, \quad \text{in fluids } j \in \{0, 1\},$$

where the normal component of the velocity and the pressure is continuous across the interface. It is possible to find an exact solution of the problem in the limit of infinitesimal harmonic perturbations of the interface. Let  $\{z = H(r, \theta, t)\}$  be the interface. We introduce the following ansatzes:

$$\mathbf{u}_j(r, \theta, z, t) = e^{i\omega t} \nabla \varphi_j, \quad \text{in fluids } j \in \{0, 1\}, \quad (45)$$

$$\varphi_1(r, \theta, z) = C_1 \cosh(k(-H_1 + z)) J_m(kr) e^{im\theta}, \quad (46)$$

$$\varphi_0(r, \theta, z) = C_0 \cosh(k(H_0 + z)) J_m(kr) e^{im\theta}, \quad (47)$$

$$H(r, \theta, t) = e^{i\omega t} h(r, \theta), \quad (48)$$

where  $J_m$  is the Bessel function of the first kind,  $m \in \mathbb{N}$ . The boundary condition at  $r = 1$  implies that  $k$  is a root of  $J_m'$ . The first roots of  $J_m'$  are reported in Table 4.

The continuity of the pressure across the interface implies that  $-i\omega \rho_1 \varphi_1 - \rho_1 g h = -i\omega \rho_0 \varphi_0 - \rho_0 g h$ . The continuity of the normal velocity implies that  $\partial_z \varphi_1(r, \theta, 0) = i\omega h(r, \theta)$  and  $\partial_z \varphi_0(r, \theta, 0) = i\omega h(r, \theta)$ . This gives the following dispersion relation:

$$\omega^2 = \frac{(\rho_0 - \rho_1) g k}{\rho_1 \coth(kH_1) + \rho_0 \coth(kH_0)}, \quad (49)$$

and the relation  $C_0 = -C_1 \sinh(kH_1)/\sinh(kH_0)$ . We perform computations with perturbations on the Fourier modes  $m = 0, 1, 2$  with the parameters  $k = k_1, k_2$  for 2 sets of density ratio  $\frac{\rho_0}{\rho_1}$ . All the tests are done with the parameters

$$H_1 = H_0 = 1, \quad R = 1, \quad g = 9.81, \quad \rho_1 = 1, \quad Re = 2 \times 10^4, \quad \eta_1 = \eta_0 = 1.$$

Note that  $g$  is used rather than  $F_r$  because there is no reference velocity. We use BDF1 time stepping with the time step  $\tau = 5 \times 10^{-3}$ . The mesh is locally refined in the vicinity of the interface: the mesh size is  $1/320$  at  $z = 0$  and  $0.1$  at  $z = \pm 1$  (there are  $19\,105 \mathbb{P}_2$  grid points in the meridian section). The fluid parameters are computed with the linear reconstruction and  $c_{\text{comp}} = 1, c_E = 1$ . The time evolution of the kinetic energy is plotted in Figure 2. The period of the motion is twice that of the kinetic energy. Theoretical and numerical angular frequencies are reported in Table 5. We recover the theoretical values up to a relative error of order 1% to 4%.

**TABLE 4** First 2 roots of  $J_m'$  for various azimuthal Fourier modes

$m$	0	1	2	3	4
$k_1$	3.8317	1.8412	3.0542	4.2012	5.3176
$k_2$	7.0156	5.3314	6.7061	8.0152	9.2824

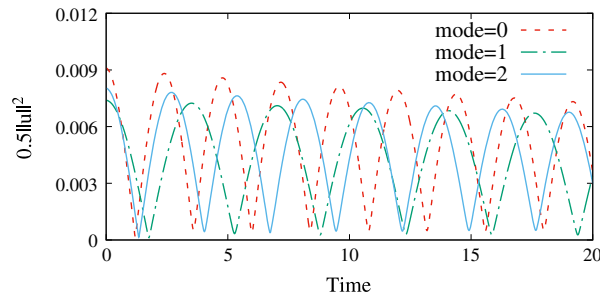


**FIGURE 2** Time evolution of the kinetic energy for density ratio  $\frac{\rho_0}{\rho_1} = 1.1$ , using wave number  $k_1$  and  $Re = 2 \times 10^4$  [Colour figure can be viewed at [wileyonlinelibrary.com](http://wileyonlinelibrary.com)]

**TABLE 5** Angular frequencies for density ratio  $\frac{\rho_0}{\rho_1} \in \{1.1, 2\}$  for azimuthal Fourier modes  $m = 0, 1, 2$ . Computations done with  $Re = 2 \times 10^4$

$m$		0			1			2		
		Exact	Num.	Rel. Err	Exact	Num.	Rel. Err	Exact	Num.	Rel. Err
$\frac{\rho_0}{\rho_1} = 1.1$	$\omega(k_1)$	1.3373	1.309	2.1E-2	0.9044	0.891	1.5E-2	1.1918	1.155	3.E-2
	$\omega(k_2)$	1.8103	1.749	3.4E-2	1.5781	1.531	3.E-2	1.7699	1.693	4.4E-2
$\frac{\rho_0}{\rho_1} = 2$	$\omega(k_1)$	3.5381	3.476	1.8E-2	2.3927	2.363	1.2E-2	3.1533	3.106	1.5E-2
	$\omega(k_2)$	4.7897	4.660	2.7E-2	4.1753	4.065	2.6E-2	4.6828	4.539	3.1E-2

## 6 | FREE SURFACE FLOW IN A ROTATING CYLINDER: NEWTON'S BUCKET

We study the problem known in the literature as Newton's bucket. The problem consists of studying a rotating bucket filled with water. Without surface tension, the geometry of the free surface is governed by the balance between gravity and the centrifugal force. At equilibrium, the free surface adopts the shape of an upward paraboloid. In the inertial frame, the velocity is purely azimuthal.

### 6.1 | Physical setting

We model this configuration by using 2 immiscible fluids of density  $\rho_0 \gg \rho_1$  contained in a closed cylinder of radius  $R$  and height  $H$  rotating at angular velocity  $\Omega$  constant with respect to an inertial frame. The 2 fluids are at rest at time  $t = 0$ , and their respective heights are  $H_0$  and  $H_1$  such that  $H = H_0 + H_1$ . Therefore, the initial interface is flat and located at  $\{z = H_0\}$ . The light fluid of density  $\rho_1$  is on top of the heavier fluid of density  $\rho_0$ . The no-slip boundary condition is enforced everywhere at the boundary of  $D$  on the velocity. No boundary condition is enforced on the level set function. We do not enforce any contact angle condition. Using the cylinder radius  $R$  as the characteristic length,  $\Omega R$  as the characteristic velocity, and the physical properties of the bottom fluid, the Froude, Reynolds, and Weber numbers are defined by

$$Fr = \frac{\Omega^2 R}{g}, \quad Re = \frac{\rho_0 \Omega R^2}{\eta_0}, \quad We = \frac{\rho_0 \Omega^2 R^3}{\kappa_{01}}. \quad (50)$$

With no surface tension effect and  $\rho_1/\rho_0 \rightarrow 0$ , the velocity field is purely toroidal:  $\mathbf{u} = r\mathbf{e}_\theta$ . The minimum water height is positive for small angular velocities ( $Fr \leq Fr^c$ ), but a dry zone appears for higher angular velocities ( $Fr > Fr^c$ ). The free surface elevation in nondimensional units is given by

$$\zeta(r) = \begin{cases} H_0 + \frac{Fr}{2} \left( r^2 - \frac{1}{2} \right) & \text{for } Fr < Fr^c, \\ \max \left( 0, \sqrt{H_0 Fr} + \frac{Fr}{2} (r^2 - 1) \right) & \text{for } Fr \geq Fr^c. \end{cases} \quad (51)$$

In our setting, the critical Froude number for no dry zone to appear is  $Fr^c = 4H_0$ . Note that this elevation does not depend on  $Re$  since the viscosity only impacts the relaxation time needed to reach equilibrium.

Since the equilibrium solution is axisymmetric, we restrict our spectral computations to the Fourier mode  $m = 0$ . All the computations of this section are done with BDF1 time stepping, linear reconstruction,  $c_{\text{comp}} = 0.5$  and  $c_E = 1$ .

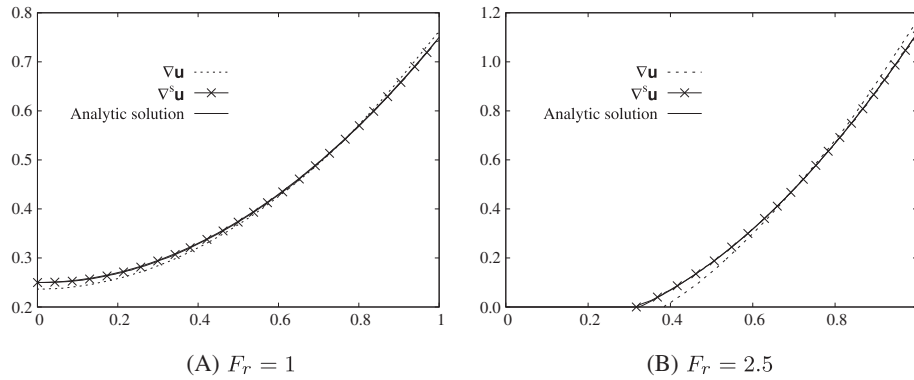


**FIGURE 3** Free surface elevation  $\zeta(r)$  for the Newton's bucket configuration: analytical solution (solid line), numerical solution with  $\nabla \mathbf{u}$  (dotted line), and numerical solution with  $\nabla^s \mathbf{u}$  (symbol  $\times$ ). A, Wet case. B, Dry case

## 6.2 | Influence of strain rate tensor

In this section, we examine the influence of the modelling of the viscous term, ie, by making the stress tensor proportional either to the gradient of the velocity  $\nabla \mathbf{u}$  alone or to the symmetric strain rate tensor  $\nabla^s \mathbf{u}$ .

We use the following parameters:  $\rho_1/\rho_0 = 10^{-3}$ ,  $\eta_1/\eta_0 = 10^{-3}$ . We have chosen  $\rho_1/\rho_0 = \eta_1/\eta_0$  to have the same Reynolds number in the 2 fluids:  $Re = 10^3$ . We perform 2 series of computations: one series with  $Fr = 1 < Fr^c$  and  $H_1 = H_0 = 0.5$  (wet case, ie, no dry zone appears) and one series with  $Fr = 2.5 > Fr^c$ ,  $H_1 = 0.5$  and  $H_0 = 0.75$  (dry case, ie, a dry zone is created). The wet case computations are performed with the time step  $\tau = 10^{-3}$ . The finite element mesh is non-uniform and composed of 46 557  $\mathbb{P}_2$  grid points in the meridian section; the  $\mathbb{P}_1$  mesh size is roughly equal to  $10^{-2}$ . The dry case computations are done with the time step  $\tau = 10^{-3}$ , and the finite element mesh is composed of 58 183  $\mathbb{P}_2$  grid points in the meridian section; the  $\mathbb{P}_1$  mesh size is roughly equal to  $10^{-2}$ .

We compare in Figure 3 the analytical solution with the 2 numerical solutions obtained with  $\nabla \mathbf{u}$  or  $\nabla^s \mathbf{u}$  in Equation 1b. The solution using  $\nabla \mathbf{u}$  is below the analytical solution for  $r < 0.6$  and above for  $r > 0.6$  (the total mass is preserved). The solution using  $\nabla^s \mathbf{u}$  is in excellent agreement with the analytical solution even near the rim of the cylinder. These results and the ones of Section 7.2 confirm that it is necessary to use the symmetric strain rate tensor when  $\eta$  is variable; the key reason is that it is not the quantity  $\left(\frac{\eta}{Re} \nabla \cdot \mathbf{u} - p\mathbf{I}\right) \cdot \mathbf{n}$  that is continuous across the interface but it is the normal stress  $\left(\frac{2\eta}{Re} \varepsilon(\mathbf{u}) - p\mathbf{I}\right) \cdot \mathbf{n}$ . These facts are well established in the literature, and if nothing else, the above test shows that the viscous tensor is well programmed with  $\nabla^s \mathbf{u}$ .

## 6.3 | Influence of the surface tension

In this section, we explore the effects of the surface tension on the surface elevation in the wet cases. The surface tension enters into the nondimensional system via the Weber number only. We set  $Re = 10^3$ ,  $Fr = 1.815$ ,  $\eta_1/\eta_0 = 6.9124$ ,  $\rho_1/\rho_0 = 0.5284$ ,  $H_0 = H_1 = 0.75$  (corresponding to the 2-fluid system considered in Brady et al<sup>30</sup> except for the kinetic Reynolds number, which is  $2 \cdot 10^3$  in Brady et al<sup>30</sup>). We consider 4 different values of the Weber number  $We = 50, 114, 550$  and  $We = \infty$  (zero surface tension). The analytical free surface profile for  $We = \infty$  is given in (51). The computations are done with  $\tau = 10^{-3}$ , and the  $\mathbb{P}_1$  mesh size is roughly equal to  $10^{-2}$  (69 841  $\mathbb{P}_2$  grid points in the meridian section).

The results are shown in Figure 4. The agreement with the results reported in figure 9 of Brady et al<sup>30</sup> is excellent. The action of the surface tension significantly modifies the profile of the free surface. The free surface flattens as the surface tension increases and a meniscus appears at the rim of the cylinder.

# 7 | FREE SURFACE FLOW IN A CYLINDER: FIXED WALLS AND ROTATING BOTTOM

## 7.1 | Physical setting

We study the flow driven by a rotating disk at the bottom of an open stationary cylindrical vessel. This configuration is modelled by using 2 immiscible fluids of density  $\rho_0 \gg \rho_1$  contained in a closed cylinder of radius  $R$  and height  $H$ . The



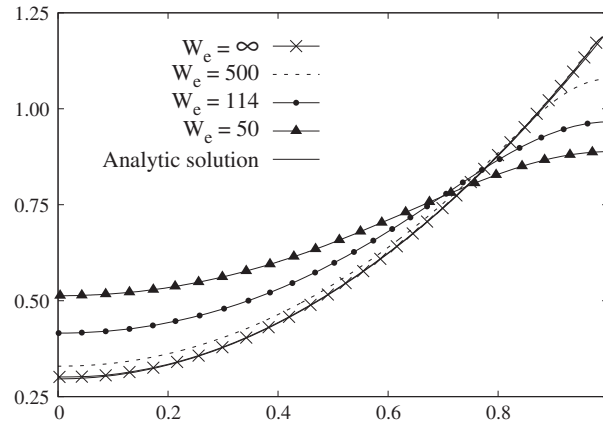


**FIGURE 4** Free surface elevation  $\zeta(r)$  for the Newton's bucket configuration using  $\nabla^s \mathbf{u}$ : analytical solution (solid line) and no surface tension (symbol  $\times$ ), with surface tension as indicated  $W_e = 50, 114, 550$ . Parameters are  $R_e = 10^3$ ,  $F_r = 1.815$ ,  $\eta_1/\eta_0 = 6.9124$ ,  $\rho_1/\rho_0 = 0.5284$ ,  $H_0 = H_1 = 0.75$

light fluid of density  $\rho_1$  is on top of the heavier fluid of density  $\rho_0$ . The bottom lid rotates at angular velocity  $\Omega$  constant with respect to an inertial frame. The lateral wall is fixed. The 2 fluids are at rest at time  $t = 0$ , and their respective heights are  $H_0$  and  $H_1$  such that  $H = H_0 + H_1$ . The no-slip boundary condition is enforced over the entire boundary of  $D$ . The initial interface is flat and located at  $\{z = H_0\}$ . Using the cylinder radius  $R$  as the characteristic length and  $\Omega R$  as the characteristic velocity and the physical properties of the bottom fluid, the Froude and the Reynolds numbers are defined by

$$F_r = \frac{\Omega^2 R}{g}, \quad R_e = \frac{\rho_0 \Omega R^2}{\eta_0}. \quad (52)$$

The steady axisymmetric solution is different from Newton's bucket paraboloid studied in the previous section since the lateral wall is motionless. We numerically compute the axisymmetric solution (ie, using only the Fourier mode  $m = 0$ ) and compare it with published numerical and experimental results.

## 7.2 | Numerics vs experiment

The free surface flow in an open cylinder with large free surface deformation has been investigated numerically and experimentally in Kahouadji et al.<sup>31</sup> The numerical method used therein consists of solving the steady axisymmetric Navier-Stokes equation projected onto a curvilinear coordinate system using a Newton-Raphson algorithm. In the experiment, the vessel is filled with car engine oil and the surface elevation is measured by using a vertical needle reflected by the free surface acting as a mirror (see details in Kahouadji et al<sup>31</sup> and Figure 5A).

We use the following parameters:  $H_1 = 0.432$ ,  $H_0 = 0.568$ ,  $\rho_1/\rho_0 = 1.409 \times 10^{-3}$ ,  $\eta_1/\eta_0 = 3.86 \times 10^{-4}$ ,  $F_r = 1.435$ , and  $R_e = 1026$ . The computations are performed with BDF1 time stepping with the time step  $\tau = 10^{-3}$ . The finite element mesh is non-uniform and composed 46 557  $\mathbb{P}_2$  grid points in the meridian section; the  $\mathbb{P}_1$  mesh size is roughly equal to  $10^{-2}$ . To limit numerical diffusion, we used  $c_E = 0.15$  in the momentum equation, and to converge faster to the steady state, we used the first-order viscosity on the level set with  $c_{\text{comp}} = 0.5$ . The reconstruction of the fluid parameters is done with (6) and  $c_{\text{reg}} = 0.5$ . The central panel in Figure 5 shows the free interface obtained by SFEMaNS using either  $\nabla \mathbf{u}$  or  $\nabla^s \mathbf{u}$  in the expression of the stress tensor; the symbol \* represent measurements. We compare in the right panel of Figure 5 the profile of the interface obtained with SFEMaNS with those from Kahouadji et al.<sup>31</sup> The agreement between SFEMaNS's profile computed with  $\nabla^s \mathbf{u}$  in the stress tensor and both the experimental data and the numerical profile obtained in Kahouadji et al<sup>31</sup> is excellent. The above computation is again a confirmation that the experimental stress tensor is well modelled by using the symmetric stress tensor.

In Figure 6, we compare the axial profiles of the velocity at  $r = 0.5$  obtained numerically in Kahouadji et al<sup>31</sup> with those obtained with SFEMaNS (using  $\nabla^s \mathbf{u}$ ). As expected, the azimuthal velocity component dominates the other 2 components and the spatial distribution of the velocity field is nontrivial. The maximum difference on the azimuthal profiles between the 2 computations is  $5 \cdot 10^{-3}$ ; the relative difference is about 2% of the maximum norm.

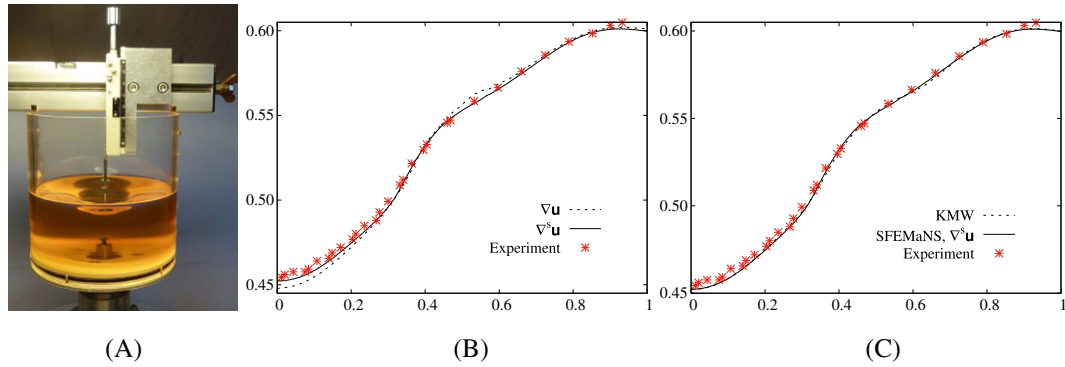


**FIGURE 5** A, Experimental set-up with the needle measuring the free surface elevation (courtesy of L. Martin Witkowski). B, Free surface elevation by SFEMaNS with  $\nabla \mathbf{u}$  (dotted line) and  $\nabla^s \mathbf{u}$  (solid line) and experimental results (symbol \*). C, Numerical solution by SFEMaNS with  $\nabla^s \mathbf{u}$  (solid line), numerical (KMW, dotted line), and experimental (symbol \*) results by Kahouadji et al<sup>31</sup> [Colour figure can be viewed at [wileyonlinelibrary.com](http://wileyonlinelibrary.com)]

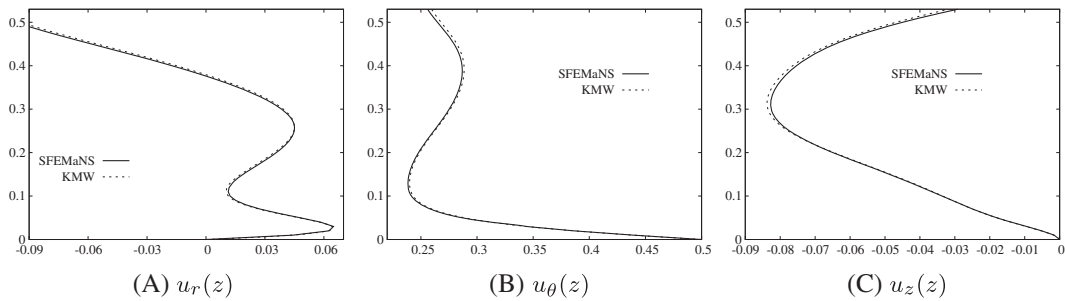


**FIGURE 6** Velocity profiles at  $r = \frac{1}{2}$  as a function of  $z$  in the oil. A,  $u_r(z)$ . B,  $u_\theta(z)$ . C,  $u_z(z)$ . Comparisons between results from SFEMaNS, using the symmetric strain rate tensor  $\nabla^s \mathbf{u}$ , and Kahouadji et al<sup>31</sup>

## 8 | BUBBLES

We investigate in this section the influence of the surface tension. We begin by studying the evolution of an axisymmetric bubble under the influence of gravity with various ratios of density and dynamical viscosity. Then we study the behaviour of an oscillating bubble without gravity.

### 8.1 | Rising bubbles

To validate the surface tension effects implemented in SFEMaNS, we start with a test case consisting of a rising axisymmetric bubble. We consider a spherical droplet of density  $\rho_1$ , initially at rest, and of radius  $R$ , in an immiscible heavier fluid of density  $\rho_0$ . We follow the evolution of the bubble under the effect of gravity. This test is important because it is well documented (see previous studies<sup>32,33</sup>).

We start with some test cases documented in Hua and Lou<sup>33</sup> where various density and viscosity ratios are investigated. The reference parameters used in the following computations are  $L_{\text{ref}} = R$  and  $U_{\text{ref}} = \sqrt{gR}$  giving

$$R_e = \frac{\rho_0 g^{1/2} R^{3/2}}{\eta_0}, \quad W_e = \frac{\rho_0 g R^2}{\kappa_{01}}, \quad F_r = 1. \quad (53)$$

Table 6 shows how to convert our definitions of  $R_e$ ,  $W_e$ , and  $F_r$  into those from Hua and Lou.<sup>33</sup> The computational domain  $D$  is a cylinder of height 24 and radius 8; the  $\mathbb{P}_1$  mesh size is  $5 \times 10^{-2}$  for  $0 \leq r \leq 2$  and 0.5 for  $r = 8$  (121 247  $\mathbb{P}_2$  grid points in the meridian section); the no-slip boundary condition is enforced everywhere at the boundary of  $D$ . The time stepping is done with BDF1 using  $\tau = 10^{-3}$ . We use only the Fourier mode  $m = 0$  since the solution is axisymmetric. These computations are performed with  $c_{\text{comp}} = 0.5$  and  $c_E = 1$ . The fluid parameters are reconstructed using (6) and  $c_{\text{reg}} = 0.5$ .

**TABLE 6** Reference parameters used for nondimensionalization in SFEMaNS and Hua and Lou<sup>33</sup> and comparison of computation parameters

Reference parameters	$L_{\text{ref}}$	$U_{\text{ref}}$	Computation parameters	$Re$	$We$	$Fr$
SFEMaNS	R	$\sqrt{gR}$	SFEMaNS	4.93	3.09	29
Hua-Lou	$D = 2R$	$\sqrt{gD}$	Hua-Lou	13.95	8.75	116

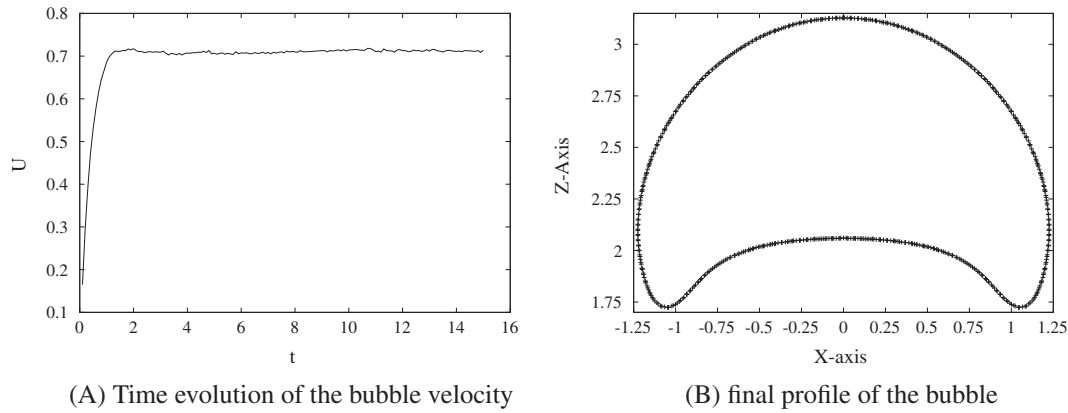


**FIGURE 7** Computation with  $\frac{\rho_0}{\rho_1} = 10^3$ ,  $\frac{\eta_0}{\eta_1} = 10^2$ ,  $Re = 4.93$ , and  $We = 29$  corresponding to  $Re = 13.95$  and  $We = 116$  in Hua and Lou<sup>33</sup>

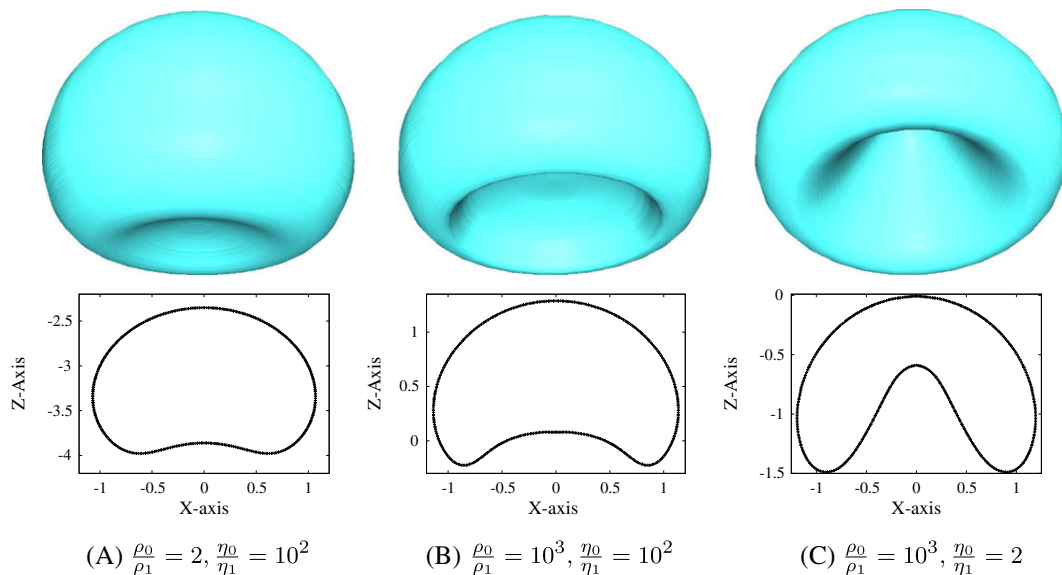


**FIGURE 8** (Top) 3D isocontour of level set ( $\phi = 0.5$ ). (Bottom) Bubble profiles along  $r$  and  $z$  axis. Computations done with  $Re = 3.09$  and  $We = 29$  and various density and viscosity ratios [Colour figure can be viewed at [wileyonlinelibrary.com](http://wileyonlinelibrary.com)]

The first test is done by setting  $Re = 4.93$ ,  $We = 29$  and using the large ratios  $\rho_0/\rho_1 = 10^3$  and  $\eta_0/\eta_1 = 10^2$ . The time evolution of the velocity of the bubble and its final shape, shown in Figure 7, are qualitatively very similar to those reported in figure 4 of Hua and Lou.<sup>33</sup> The relative difference on the terminal velocity of the bubble is 0.6% ( $0.714$  versus  $0.502 \times \sqrt{2} = 0.71$ ), and the height and width of the bubble match the values reported in Hua and Lou.<sup>33</sup>

In the second test, we set  $Re = 3.09$  and  $We = 29$ , and we investigate the influence of the density and viscosity ratios. The density and viscosity ratios studied are  $\{2, 10^3\}$  and  $\{2, 10^2\}$ , respectively. The final shape of the bubble is shown in Figure 8, and the final velocity of the bubble is reported in Table 7. These results can be compared to figures 17 and 19, and figures 18 and 20 of Hua and Lou.<sup>33</sup> The overall shape (height and width) is well reproduced. The relative differences on the final velocity are between 0.2% and 5%. We conclude that our method correctly approximates axisymmetric problems with surface tension effects.

**TABLE 7** Final velocity  $\frac{U}{(gR)^{1/2}}$  with  $R_e = 3.09$  and  $W_e = 29$ 

Fluid parameters	$\frac{\rho_0}{\rho_1} = 2, \frac{\eta_0}{\eta_1} = 10^2$	$\frac{\rho_0}{\rho_1} = 10^3, \frac{\eta_0}{\eta_1} = 10^2$	$\frac{\rho_0}{\rho_1} = 10^3, \frac{\eta_0}{\eta_1} = 2$
Final bubble velocity (SFEMaNS)	0.345	0.586	0.487
Final bubble velocity (Hua-Lou)	0.346	0.585	0.513
Relative difference	0.2%	0.3%	5.1%

## 8.2 | Oscillating bubbles

We now study how a bubble immersed in a quiescent fluid with no gravity oscillates. It is again a classical test case (number 5 in Lemonnier et al<sup>32</sup>). The inner and outer fluids are immiscible and of density  $\rho_1$  and  $\rho_0$ , respectively. The initial perturbations of the spherical shape of radius  $R$  are supposed to be small, and, in the case of inviscid fluids, the analytical formula for the oscillation frequency and shape of the interface are given in Lamb<sup>34</sup>:

$$\omega_n^2 = \frac{n(n+1)(n-1)(n+2)}{(n+1)\rho_1 + n\rho_0} \frac{\kappa_{01}}{R^3}, \quad r_s(\theta, \chi, t) = R[1 + \epsilon Y_{mn} \sin(\omega_n t)], \quad (54)$$

here,  $\epsilon$  is the amplitude of the perturbation and  $Y_{mn}$  are the spherical harmonics:

$$Y_{mn}^o = \sin(m\theta)P_n^m(\cos \chi), \quad Y_{mn}^e = \cos(m\theta)P_n^m(\cos \chi), \quad (55)$$

where  $n \in \mathbb{N}$ ,  $m$  is the azimuthal Fourier mode,  $\theta$  the azimuth,  $\chi$  the colatitude, and  $P_n^m$  the Legendre functions.

We neglect gravity and use the radius of the initial spherical bubble  $R$  as the characteristic length scale and the physical properties of the inner fluid as reference properties. We define the Ohnesorge number that relates the viscous forces to inertial and surface tension forces:

$$\text{Oh} = \eta_1 / \sqrt{\rho_1 R \kappa_{01}}. \quad (56)$$

Note that viscosity effects decrease when Oh decreases.

We set  $\rho_0/\rho_1 = 1$ ,  $\eta_0/\eta_1 = 1$  and focus on perturbations on the mode  $n = 2$ . We perform axisymmetric computations with various values of  $\text{Oh} \in \{0.05, 0.02, 0.01, 0.002, 0.001\}$  and a perturbation on the Fourier  $m = 0$  along the spherical harmonics  $Y_{02}$  with  $\epsilon = \{0.1, 0.5\}$ . The computational domain  $D$  is a sphere of radius 40. The no-slip boundary condition is enforced everywhere at the boundary of  $D$ . The computations are done with BDF1 time stepping with  $\tau = 10^{-3}$ . The  $\mathbb{P}_1$  mesh size is  $4 \times 10^{-2}$  in the bubble ( $r^2 + z^2 \leq 1$ ) and 10 at the boundary of  $D$  (51 877  $\mathbb{P}_2$  grid points in the meridian section). The compression coefficient  $c_{\text{comp}}$  is set to 0.5 and the entropy coefficient  $c_E = 1$ . The fluid parameters are computed with a linear reconstruction. The theoretical period from (54) is  $T = 2.9$ .

We show in the left panel of Figure 9 the time evolution of the  $L^2$ -norm of the velocity Fourier mode  $m = 0$  computed in SFEMaNS with  $\text{Oh} \in \{0.05, 0.02, 0.01, 0.002, 0.001\}$ . We observe that the signal varies in time with the expected half period. Note that we recover the theoretical value of the frequency only for  $\text{Oh} \leq 0.002$ ; for larger values of the Ohnesorge number, the oscillations are slower due to viscous effects, eg, for  $\text{Oh} = 0.05$ , the period is around 3.3, which is 13% higher than the theoretical inviscid period.

We also perform fully 3D computations using 32 complex Fourier modes with the perturbation  $\epsilon = 0.1$  on the Fourier mode  $m = 1$  on the spherical harmonics  $Y_{12}$ . Since the theoretical frequency (54) does not depend on the azimuthal mode number, we should recover the period  $T = 2.9$  obtained in the axisymmetric computations. We show in the right panel of Figure 9 the time evolution of the  $L^2$ -norm of the Fourier  $m = 1$  of the velocity for  $\text{Oh} \in \{0.02, 0.01, 0.002\}$ . As expected, we observe that for  $\text{Oh} = 0.002$ , the period is close to 2.9 with a 5% error range.

We now investigate the effect of a large initial deformation  $\epsilon = 0.5$  in the axisymmetric configuration, ie, the perturbation is done on the spherical harmonics  $Y_{02}$ . We show in Figure 10 the time evolution of the radial velocity obtained with  $\epsilon = 0.5$  and  $\epsilon = 0.1$ . The non-linear effects are large when  $\epsilon = 0.5$ ; as a result, the period and the amplitude of the oscillations are increased. Snapshots of the bubble are shown in the top right and bottom panels of Figure 10.

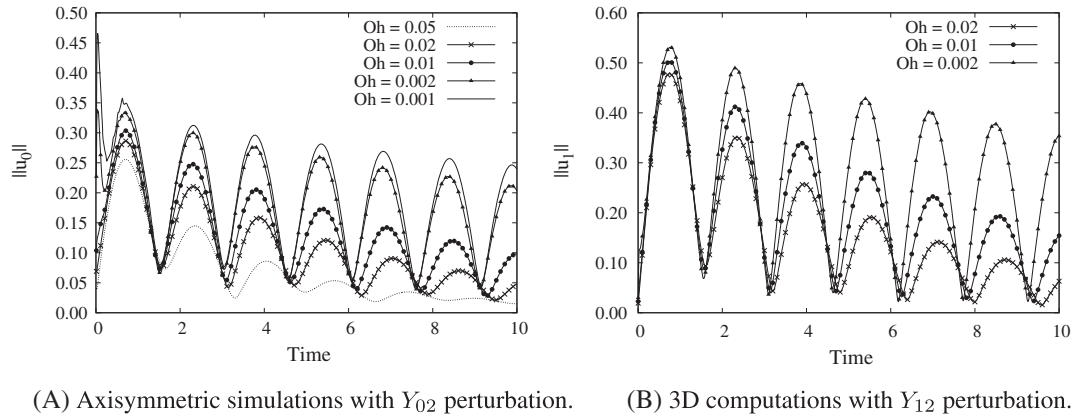


**FIGURE 9** Time evolution of the  $L^2$ -norm of A, velocity mode  $m = 0$  and B, velocity mode  $m = 1$  for  $\epsilon = 0.1$  at different Ohnesorge numbers

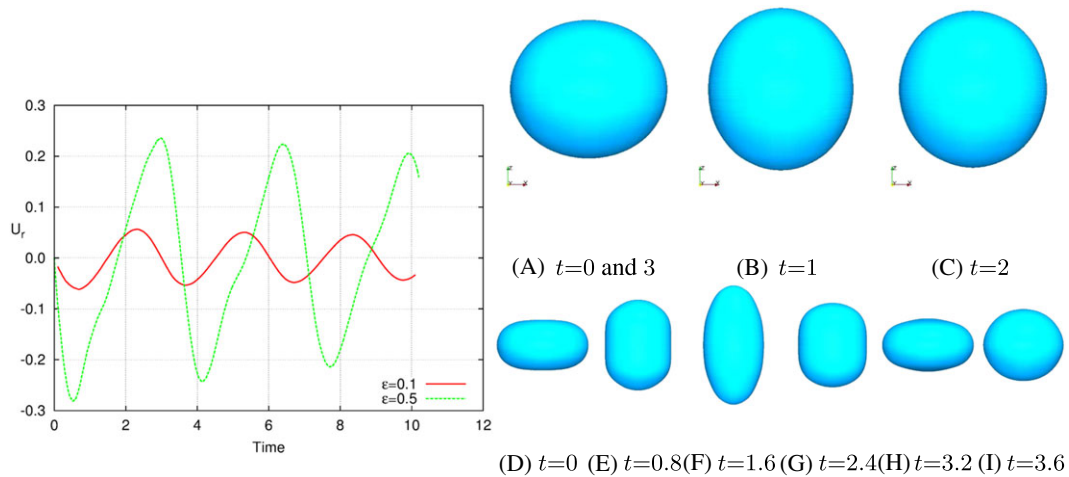


**FIGURE 10** Left: Time evolution of the radial velocity of the  $m = 0$  mode for  $\epsilon = 0.1$  and  $\epsilon = 0.5$  at  $Re_{st} = 500$ . Right: Snapshots of the bubble for  $\epsilon = 0.1$  (A-C) and  $\epsilon = 0.5$  (D-I) [Colour figure can be viewed at [wileyonlinelibrary.com](http://wileyonlinelibrary.com)]

## 9 | MPR INSTABILITY

In this section, we numerically simulate the MPR instability that can sometimes be observed in Hall-Héroult cells in aluminium production facilities. This 2-phase magnetohydrodynamical instability drives a rotating gravity wave. Here, it defines a three-dimensional test-case for our magnetohydrodynamical multiphase solver.

### 9.1 | Description of the MPR instability

Aluminium is produced by electrolysis in large factories that gather hundreds of Hall-Héroult cells organized around a central current loop. The fluid in each cell is stratified in 2 layers: The bottom layer is composed of molten aluminium and the top layer is composed of cryolite, which is a molten salt with dissolved alumina. Both fluid layers are very shallow, only 5 to 30 cm high, but 4 to 10 m wide. The electrolysis requires an electrical current  $\mathbf{J}$  that runs vertically through the cell and may reach magnitude of the order  $J \sim 1.0 \times 10^4 \text{ A/m}^2$  (Evans and Ziegler<sup>35</sup>). In the factory, there is always a background magnetic field, of typical magnitude  $B \sim 1$  to 10 mT. The interplay of this strong current density and the background magnetic field leads to a spontaneous appearance of long wavelength gravity waves on the fluid interface that can reach large amplitudes. This phenomenon is often called in the literature “metal pad instability” or “metal pad roll instability” (MPR). In practice, this instability can be avoided if the cryolite layer is thick enough, but since the cryolite’s conductivity is low, this entails larger resistive losses that further increase the already high power consumption of Al factories. Therefore, understanding and controlling the MPR instability has obvious industrial applications and has motivated intense research on this topic since the 1980s.

Laboratory experiments are difficult to realize because they need to deal with high temperatures, except for Pedchenko et al<sup>36</sup> who designed a clever experiment that operates at room temperature. More recently, several groups performed direct three-dimensional numerical simulations of the MPR instability in realistic fluid domains. Gerbeau et al<sup>37</sup> use a finite element ALE method, Steiner<sup>38</sup> a finite volume ALE method, and Munger<sup>39</sup> a finite volume level set method. To the best of our knowledge, a hybrid Fourier finite element method with level set approximation as the one presented in this paper has never been tried before on this problem.

## 9.2 | Physical configuration

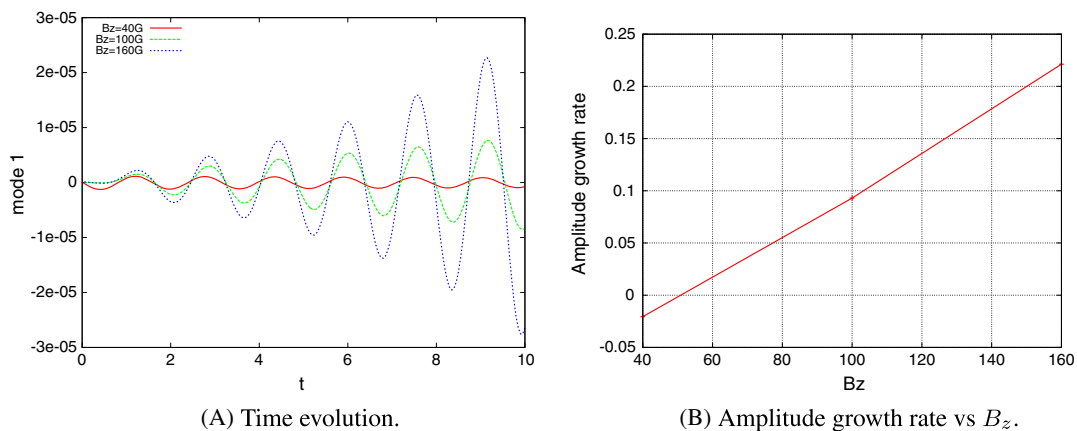
For numerical reasons, we are limited to the simulation of MPR in cells with cylindrical geometry. Currently, there is no quantitative theory that allows a critical comparison, but cylindrical cells have been studied numerically in Gerbeau et al<sup>37</sup> and Steiner.<sup>38</sup> In Steiner,<sup>38</sup> MPR is found within in a small cylindrical crucible  $D$  with radius  $R = 0.035\text{m}$  and height  $H = 0.15\text{m}$ . Cryolite and aluminium layers have equal heights  $H_0 = H_1 = 0.075\text{m}$ . The density, conductivity, and kinematic viscosity of both fluids are

$$\begin{aligned}(\rho_0, \sigma_0, \nu_0) &= (2300 \text{ kg/m}^3, 3.5 \times 10^6 \text{ Sm}^{-1}, 5.2 \times 10^{-7} \text{ m}^2/\text{s}), \\(\rho_1, \sigma_1, \nu_1) &= (2150 \text{ kg/m}^3, 2.5 \times 10^2 \text{ Sm}^{-1}, 1.2 \times 10^{-6} \text{ m}^2/\text{s}).\end{aligned}\tag{57}$$

Since it can be shown theoretically by using linear stability arguments that the instability threshold converges to a finite limit when the ratio  $\sigma_1/\sigma_0$  goes to zero, to avoid using extremely fine grids, we use in our computations the value  $\sigma_1 = 3.5 \times 10^4 \text{ Sm}^{-1}$  instead of  $2.5 \times 10^2 \text{ Sm}^{-1}$ . The numerical value of the ratio  $\sigma_1/\sigma_0$  is  $10^{-2}$ , which is a good approximation of 0 (the actual ratio is  $7.1 \times 10^{-5}$ ). As before, the index  $_0$  refers to the bottom layer, here the aluminium, and the index  $_1$  refers to the top layer, here the cryolite. At equilibrium, we suppose a homogenous current density  $\mathbf{J} = J\mathbf{e}_z$ . The magnetic field is  $\mathbf{B} = (\mu_0 J r/2)\mathbf{e}_\theta + B_z\mathbf{e}_z$  and combines the azimuthal magnetic field generated by the current with an external homogenous vertical magnetic field from the background magnetic field. We vary  $B_z$  in the range  $4 \times 10^{-3}$  to  $1.60 \times 10^{-2} \text{ T}$  while keeping  $J = 2 \times 10^4 \text{ A/m}^2$ . We ignore surface tension effects, and gravity is  $g = 9.81\text{m/s}^2$ . In this section, we use the dimensional version of SFEMaNS.

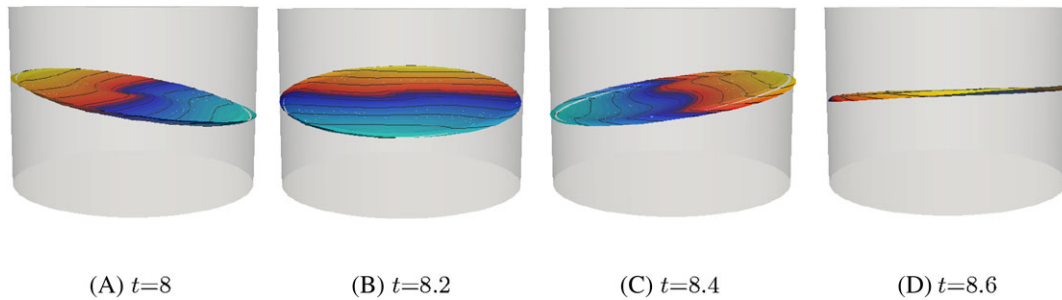
The computations are done with BDF1 time stepping with  $\tau = 5 \times 10^{-3}\text{s}$ . The no-slip boundary condition is enforced at  $\partial D$ . The  $\mathbb{P}_1$  mesh size is  $0.00075\text{m}$  near the interface and  $0.0035\text{m}$  at the boundary of the computational domain (14077  $\mathbb{P}_2$  grid points in the meridian section).  $\mathbb{P}_2$  elements are used for the level set. The compression coefficient  $c_{\text{comp}}$  is set to 0.5 and the entropy coefficient  $c_E = 1$ . The fluid parameters are computed with the linear reconstruction.

Figure 11 shows the appearance of the MPR instability for the fixed current  $J = 2 \times 10^4 \text{ A/m}^2$  when  $B_z$  increases. The left panel shows the time evolution of the Fourier coefficient of the  $m = 1$  mode of the radial component of the velocity for a point near the rim of the cylinder. Oscillations occur with a period of the order of the gravity wave period (namely,  $T = 1.5 \text{ s}$  here), their amplitude decreases for  $B_z = 4 \times 10^{-3} \text{ T}$  and increases beyond. The threshold is determined with the amplitude growth rate of  $\|\mathbf{u}(m = 1)\|_{L^2}$  from Figure 11B as being  $B_z^c \approx 5 \times 10^{-3} \text{ T}$ .



**FIGURE 11** Metal pad roll instability. A, Time evolution of the Fourier coefficient of the  $m = 1$  mode of the radial velocity for a point near the rim of the cylinder for different  $B_z$  and fixed  $J = 2 \times 10^4 \text{ A/m}^2$ . B, Amplitude growth rate of  $\|\mathbf{u}(m = 1)\|_{L^2}$  as a function of  $B_z$  [Colour figure can be viewed at [wileyonlinelibrary.com](http://wileyonlinelibrary.com)]





**FIGURE 12** Snapshots of the interface's height between the 2 fluids at different time instants viewed in perspective for about half a period. A cylinder of radius 0.035 m and height 0.05 m is indicated in light grey. Computations are done with  $J = 2 \times 10^4 \text{ A/m}^2$  and  $B_z = 1.6 \times 10^{-2} \text{ T}$  [Colour figure can be viewed at [wileyonlinelibrary.com](http://wileyonlinelibrary.com)]

Figure 12 shows the interface at different times in the saturated regime for  $J = 2 \times 10^{-4} \text{ A/m}^2$  and  $B_z^c = 1.6 \times 10^{-2} \text{ T}$ . The crest rotates clockwise as expected since  $JB_z > 0$  (see Sele<sup>40</sup>).

## 10 | CONCLUSION

A new time stepping technique using the momentum as dependent variable to solve incompressible multiphase problems has been introduced and validated. The method is partially inspired from Guermond et al.<sup>7</sup> The key advantage of this approach is that the mass matrix is time-independent, which makes this technique suitable for spectral methods. The method has been validated by solving a wide range of problems going from manufactured solutions and benchmark tests to a magnetohydrodynamical problem of great importance for the industrial production of aluminium. This test case demonstrates the capability of our non-linear approach to simulate complex MHD phenomena. We are currently working on parametric studies to measure the impact of the different parameters in the MPR instability (current, background field, and geometrical dimensions). This analysis should have practical implications in the study of the MPR instability in Hall-Héroult cells and other processes where MHD plays some role like in liquid metal batteries (see, eg, Herreman et al<sup>6</sup>).

## ACKNOWLEDGEMENTS

This material is based upon work supported by the National Science Foundation grants DMS-1620058 and DMS-1619892, by the Air Force Office of Scientific Research, USAF, under grant/contract number FA9550-15-1-0257, and by the Army Research Office under grant/contract number W911NF-15-1-0517. This work was granted access to the HPC resources of IDRIS under the allocation 2016-0254 made by GENCI (Grand Equipement National de Calcul Intensif) in France. L. Cappanera is thankful to Texas A&M University and LIMSI, CNRS, for their financial support.

## ORCID

Loïc Cappanera  <http://orcid.org/0000-0002-3871-1073>

## REFERENCES

1. Dong S, Shen J. A time-stepping scheme involving constant coefficient matrices for phase-field simulations of two-phase incompressible flows with large density ratios. *J Comput Phys.* 2012;231(17):5788-5804.
2. Anderson DM, McFadden GB, Wheeler AA. Diffuse-interface methods in fluid mechanics. *Annual review of fluid mechanics*, Vol. 30. Annu Rev Fluid Mech, Vol. 30. Palo Alto, CA: Annual Reviews; 1998:139-165.
3. Lowengrub J, Truskinovsky L. Quasi-incompressible Cahn-Hilliard fluids and topological transitions. *R Soc Lond Proc Ser A Math Phys Eng Sci.* 1998;454(1978):2617-2654.
4. Gurtin ME, Polignone D, Viñals J. Two-phase binary fluids and immiscible fluids described by an order parameter. *Math Models Methods Appl Sci.* 1996;6(6):815-831.
5. Shen J, Yang X. A phase-field model and its numerical approximation for two-phase incompressible flows with different densities and viscosities. *SIAM J Sci Comput.* 2010;32(3):1159-1179.
6. Herreman W, Nore C, Cappanera L, Guermond JL. Tayler instability in liquid metal columns and liquid metal batteries. *J Fluid Mechanics.* 2015;771:79-114.



7. Guermond JL, Salgado AJ, Shen J. Splitting for variable density flows. *SIAM J Numer Anal.* 2017. In preparation.
8. Kuzmin D, Löhner R, Turek S. *Flux-Corrected Transport*, Scientific Computation. New York City, USA: Springer; 2005. 3-540-23730-5.
9. Boris JP, Book DL. Flux-corrected transport. I. SHASTA, a fluid transport algorithm that works [J. Comput. Phys. 11 (1973), no. 1, 38–69]. *J Comput Phys.* 1997;135(2):170-186. With an introduction by Steven T. Zalesak, Commemoration of the 30th anniversary of J. Comput. Phys.
10. Zalesak ST. Fully multidimensional flux-corrected transport algorithms for fluids. *J Comput Phys.* 1979;31(3):335-362.
11. Bell JB, Marcus DL. A second-order projection method for variable-density flows. *J Comput Phys.* 1992;101:334-348.
12. Almgren AS, Bell JB, Colella P, Howell LH, Welcome ML. A conservative adaptive projection method for the variable density incompressible Navier-Stokes equations. *J Comput Phys.* 1998;142(1):1-46.
13. Pyo JH, Shen J. Gauge-Uzawa methods for incompressible flows with variable density. *J Comput Phys.* 2007;221(1):181-197.
14. Guermond JL, Quartapelle L. A projection FEM for variable density incompressible flows. *J Comput Phys.* 2000;165(1):167-188.
15. Guermond JL, Salgado A. A splitting method for incompressible flows with variable density based on a pressure Poisson equation. *J Comput Phys.* 2009;228(8):2834-2846.
16. Guermond JL, Salgado AJ. Error analysis of a fractional time-stepping technique for incompressible flows with variable density. *SIAM J Numer Anal.* 2011;49(3):917-944.
17. Guermond JL, Pasquetti R, Popov B. Entropy viscosity method for nonlinear conservation laws. *J Comput Phys.* 2011;230(11):4248-4267.
18. Harten A. The artificial compression method for computation of shocks and contact discontinuities. III. Self-adjusting hybrid schemes. *Math Comp.* 1978;32:363-389.
19. Sethian JA. A fast marching level set method for monotonically advancing fronts. *Proc Natl Acad Sci USA.* 1996;93:1591-1595.
20. Olsson E, Kreiss G. A conservative level set method for two phase flow. *J Comput Phys.* 2005;210:225-246.
21. Coupez T. Convection of Local Level Set Function for Moving Surfaces And Interfaces in Forming Flow. In: AIP Conference Proceedings César de Sá JMA, Santos AD, eds., Vol. 908. College Park, Maryland, USA; 2007. (1).
22. Coupez T, Silva L, Ville L. Convected level set method for the numerical simulation of fluid buckling. *Internat J Numer Methods Fluids.* 2010February;66:324-344.
23. Guermond JL, de Luna MQ, Thompson T. An conservative anti-diffusion technique for the level set method. *J Comput Appl Math.* 2017;321:448-468.
24. Frigo M, Johnson SG. The design and implementation of FFTW3. *Proc of the IEEE.* 2005;93(2):216-231.
25. Karypis G, Kumar V. A fast and high quality multilevel scheme for partitioning irregular graphs. *SIAM J Sci Comput.* 1998;20(1):359-392.
26. Balay S, Abhyankar S, Adams MF, othres. PETSc users manual. ANL-95/11 - Revision 3.5, Argonne National Laboratory; 2014.
27. Guermond JL, Laguerre R, Léorat J, Nore C. An interior penalty Galerkin method for the MHD equations in heterogeneous domains. *J Comput Phys.* 2007;221(1):349-369.
28. Guermond JL, Laguerre R, Léorat J, Nore C. Nonlinear magnetohydrodynamics in axisymmetric heterogeneous domains using a Fourier/finite element technique and an interior penalty method. *J Comput Phys.* 2009;228:2739-2757.
29. Guermond JL, Léorat J, Luddens F, Nore C, Ribeiro A. Effects of discontinuous magnetic permeability on magnetodynamic problems. *J Comput Phys.* 2011;230:6299-6319.
30. Brady PT, Herrmann M, Lopez JM. Two-fluid confined flow in a cylinder driven by a rotating end wall. *Phys Rev E.* 2012;85:016308.
31. Kahouadji L, Martin Witkowski L. Free surface due to a flow driven by a rotating disk inside a vertical cylindrical tank: axisymmetric configuration. *Phys of Fluids.* 2014;26(7):072105.
32. Lemonnier H, Jamet D, Lebaigue O. *Validation of Advanced Computational Methods for Multiphase Flow.* 1st edition, Vol. ISBN: 1-56700-218-8. Danbury, Connecticut, USA: Begell house, Inc.; 2005.
33. Hua J, Lou J. Numerical simulation of bubble rising in viscous liquid. *J Comput Phys.* 2007;222(2):769-795.
34. Lamb SirHorace. *Hydrodynamics.* 6th edition, Vol. isbn: 9780521458689. Cambridge (UK): Cambridge Mathematical library; 1993.
35. Evans JW, Ziegler DP. The electrolytic production of aluminum. *Encyclopedia of Electrochemistry.* 2007.
36. Pedchenko A, Molokov S, Priede J, Lukyanov A, Thomas PJ. Experimental model of the interfacial instability in aluminium reduction cells. *EPL (Europhysics Letters).* 2009;88(2):24001.
37. Gerbeau JF, Lelièvre T, Le Bris C. Simulations of MHD flows with moving interfaces. *J Comput Phys.* 2003;184(1):163-191.
38. Steiner G. Simulation numérique de phénomènes MHD. *Ph.D. Thesis;* 2009.
39. Munger D. Stabilité magnétohydrodynamique des cuves d'électrolyse: aspects physiques et idées nouvelles. *Ph.D. Thesis;* 2008.
40. Sele T. Instabilities of the metal surface in electrolytic alumina reduction cells. *Metallurgical Trans B.* 1977;8(3):613-618.

**How to cite this article:** Cappanera L, Guermond J-L, Herreman W, Nore C. Momentum-based approximation of incompressible multiphase fluid flows. *Int J Numer Meth Fluids.* 2018;86:541–563. <https://doi.org/10.1002/fld.4467>